Interlibrary Loans and Journal Article Requests

Notice Warning Concerning Copyright Restrictions:

The copyright law of the United States (Title 17, United States Code) governs the making of photocopies or other reproductions of copyrighted materials.

Under certain conditions specified in the law, libraries and archives are authorized to furnish a photocopy or other reproduction. One specified condition is that the photocopy or reproduction is not to be *"used for any purpose other than private study, scholarship, or research."* If a user makes a request for, or later uses, a photocopy or reproduction for purposes in excess of "fair use," that user may be liable for copyright infringement.

Upon receipt of this reproduction of the publication you have requested, you understand that the publication may be protected by copyright law. You also understand that you are expected to comply with copyright law and to limit your use to one for private study, scholarship, or research and not to systematically reproduce or in any way make available multiple copies of the publication.

The Stephen B. Thacker CDC Library reserves the right to refuse to accept a copying order if, in its judgment, fulfillment of the order would involve violation of copyright law.

Terms and Conditions for items sent by e-mail:

The contents of the attached document may be protected by copyright law. The CDC copyright policy outlines the responsibilities and guidance related to the reproduction of copyrighted materials at CDC. If the document is protected by copyright law, the following restrictions apply:

- You may print only one paper copy, from which you may not make further copies, except as maybe allowed by law.
- You may not make further electronic copies or convert the file into any other format.
- You may not cut and paste or otherwise alter the text.

Polymer 264 (2023) 125407

Contents lists available at ScienceDirect

Polymer

journal homepage: www.elsevier.com/locate/polymer

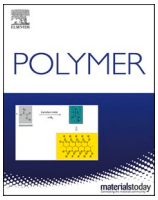

Dispersion of modified fumed silica in elastomeric nanocomposites

Ugochukwu Okoli [a,1], Kabir Rishi [b,1], Gregory Beaucage [a,*], Hendrik K. Kammler [c], Alex McGlasson [d], Michael Chauby [e], Vishak Narayanan [f], James Grammens [a], Vikram K. Kuppa [g]

[a] Chemical & Materials Engineering, University of Cincinnati, Cincinnati, OH, 45221, USA
[b] Centers for Disease Control and Prevention, National Institute for Occupational Safety and Health, Cincinnati, OH, 45213, USA
[c] Novartis Pharma AG, Postfach, CH-4002, Basel, Switzerland
[d] Polymer Science & Engineering, University of Massachusetts, Amherst, MA, 01003, USA
[e] Chemical Engineering, Drexel University, Philadelphia, PA, 19104, USA
[f] Reliance Industries Ltd., Elastomer Business Group, Navi Mumbai, Maharashtra, 400701, India
[g] Nonstructural Materials Division, University of Dayton Research Institute, Dayton, OH, 45469, USA

A B S T R A C T

In polymer nanocomposites, surface modification of silica aggregates can shield Coulombic interactions that inhibit agglomeration and formation of a network of agglomerates. Surface modification is usually achieved with silane coupling agents although carbon-coating during pyrolytic silica production is also possible. Pyrogenic silica with varying surface carbon contents were dispersed in styrene-butadiene (SBR) rubber to explore the impact on hierarchical dispersion, the emergence of meso-scale structures, and the rheological response. Pristine pyrogenic silica aggregates at concentrations above a critical value (related to the Debye screening length) display correlated meso-scale structures and poor filler network formation in rubber nanocomposites due to the presence of silanol groups on the surface. In the present study, flame synthesized silica with sufficient surface carbon monolayers can mitigate the charge repulsion thereby impacting network structural emergence. The impact of the surface carbon on the van der Waals enthalpic attraction, a^*, is determined. The van der Waals model for polymer nanocomposites is drawn through an analogy between thermal energy, k_BT, and the accumulated strain, γ. The rheological response of the emergent meso-scale structures depends on the surface density of both carbon and silanol groups.

1. Introduction

Nanoscale silica is produced either by wet synthesis, such as precipitated silica, or thermally, such as pyrogenic, or fumed silica. High-temperature thermal synthesis is achieved via flame, ovens, electric or plasma arcs. Commercial flame synthesis involves the pyrolysis of silicon tetrachloride in an oxygen-rich atmosphere to produce fumed silica. Precipitated silica is commercially produced by acid neutralization of water glass (sodium silicate solutions). Silica nanoparticles have been extensively applied in a wide range of fields from tires to filtration media [1–3]. In tires, wet grip and rolling resistance are two essential properties. Wet grip is related to handling on a wet road and is measured in a dynamic mechanical or oscillatory shear experiment by higher tanδ values at 0 °C and 1 Hz [4]. Rolling resistance is associated with energy loss induced by the deformation of the contact area and the damping properties and is improved with lower tanδ values at 60 °C and 1 Hz [5–8]. Consequently, a goal in tire research is to reach a compromise between reduced tanδ values at 60 °C and increased tanδ values at 0 °C [9].

Dispersion of nanoparticles (estimated through the molar second virial coefficient, B_2, discussed later) in viscous polymers is dictated by mixing kinetics [10,11], filler-matrix interfacial compatibility (for example silane treatment of nano-silica [12–15], organophilization of montmorillonite [16,17], and acrylate treatment of olive stone waste [18]), the interaction potentials between particles [19,20], and matrix viscosity [21]. Nanofillers such as silica impact the properties of elastomeric nanocomposites. The literature reports that poor dispersion hinders the enhancement to properties such as modulus and tear resistance [22–24], although it has been argued that the influence of the state of dispersion on nanocomposite properties is tied to the physical state of the polymer (glassy/melt) [25]. In a simplistic view, poor dispersion might result from clustering and agglomeration of nanoaggregates to minimize their surface area. However, the situation is more nuanced since the structure of fillers in elastomers is multi-hierarchical relying on local clustering of aggregates of primary particles [20,26,27]. These local clusters agglomerate into a micron-scale filler network that enhances tear resistance and conductivity [28–32]. Dispersion on these multiple size scales can be influenced by processing and by

* Corresponding author.
E-mail address: beaucag@uc.edu (G. Beaucage).
[1] Equal contribution by U.O. & K.R.

https://doi.org/10.1016/j.polymer.2022.125407
Received 31 July 2022; Received in revised form 25 September 2022; Accepted 6 October 2022
Available online 11 October 2022
0032-3861/

compatibilization, leading to a complex structural emergence.

Rubber has a low dielectric constant, so it is not expected to observe Coulombic repulsion between embedded filler particles. However, it was recently found that Coulombic repulsion between aggregates of unmodified silica at filler concentrations above a critical value associated with the Debye screening length does, in fact, occur in typical elastomeric compounds [19]. It might be expected that Coulombic repulsion of nanoaggregates would improve dispersion and therefore enhance properties. To the contrary, this type of local dispersion is detrimental to nanocomposite properties since it prevents the formation of local aggregate clusters, and hence a network of these clusters on macroscopic scales [26–32]. For this reason, it is desirable to prevent Coulombic repulsions between silica aggregates as depicted in Fig. 1(a), thereby, enhancing nanoscale dispersion (large B_2) and allowing the formation of clusters of aggregates that can assemble into an emergent macroscopic network (larger correlation length, ξ) as shown in Fig. 1(b). Filler nanoparticles are immiscible in the polymer matrix which results in the formation of these clusters of repulsive particles and repulsion opposes the natural tendency to phase separate resulting in a locally correlated system in Fig. 1(a). Bulk separation of filler is opposed by the accumulated strain. Immiscibility and kinetic dispersion also drive network formation in the absence of surface charges on nanoparticles in Fig. 1(b). In both cases, charged and uncharged aggregates, the equilibrium state would be completely phase-separated particles.

1.1. Surface modification of silica

The density of surface silanol functional groups on silica, schematically shown in Fig. 2(a), dictates the extent of surface electrostatic charges that affect the extent of repulsive Coulombic interactions between nanoaggregates. These correlations present a correlation peak in X-ray scattering (described below) [19,20]. Surface modification of silica involves reacting silanol moieties with neutral functional groups like hexamethyldisilazane, shown in Fig. 2(b), dimethyldichlorosilane, and polymethylhydrosiloxane [33]. Neutral particles do not have specific Coulombic interactions, will not correlate, and their interactions can be approximated by a mean-field, as discussed below [19]. The surface of fumed silica particles is characterized by the presence of the isolated silanols, neighboring hydrogen-bonded vicinal silanols and siloxanes, and geminal silanols that share a silicon atom and are too close to hydrogen bond together, statistically distributed over the surface. For CaboSil®, a commercial grade of fumed silica, the geminal and isolated silanols on the surface were estimated to be about 20% and 43%, respectively whereas the rest are comprised of siloxanes as measured through ^{29}Si CP-MAS spectroscopy [34]. Similarly, silica gel which is akin to precipitated silica had about 10% geminal and 61% isolated silanols indicating that the total silanol content is approximately equal for both types of silica, although many of these silanol groups are also hydrogen bonded [34]. Owing to these polar silanol moieties on the surface, fumed silica, on the nanoscale, is incompatible with non-polar hydrocarbon polymer matrices [35–37]. Further, with repulsive surface charge, particles cannot cluster so a weakly ordered array of ramified aggregates results at sufficient concentration for charge interaction, that is for aggregate separation distances smaller than the Debye screening length [19].

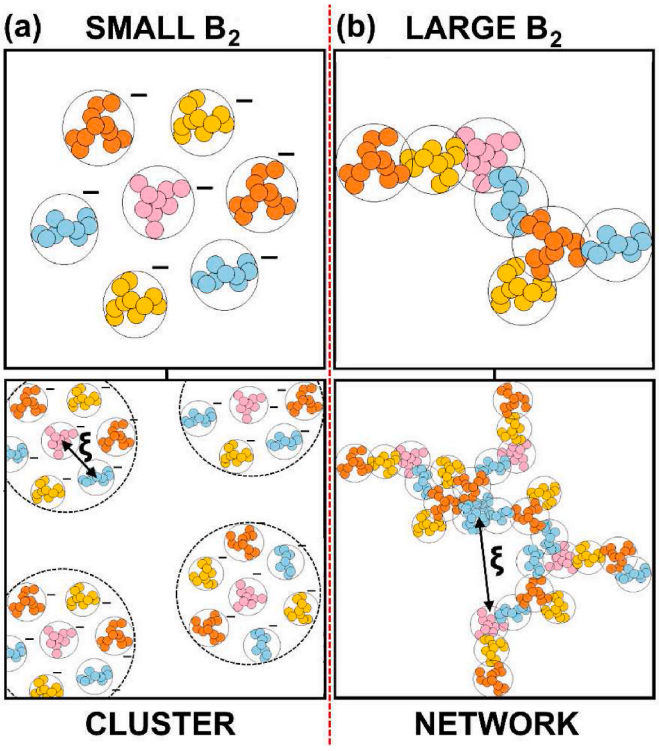

Fig. 1. (a) Silica aggregates with charge dispersion and specific interactions. (b) Clusters of aggregates that display mean field interactions between aggregates on the nanoscale. ξ indicates the correlation length. Nanoscale Coulombic repulsion prevents formation or agglomerates of aggregates and the resulting agglomerate network formation at macroscopic scales required for improvement in performance.

Dispersion of silica nanofillers in elastomer is generally enhanced by the introduction of a silane coupling agent during melt compounding, Fig. 2(b) [22,38–41]. The intent is to improve filler-polymer interactions. Grades of pyrogenic silica are available with chemically treated surfaces adding carbon functionality or short-chain hydrocarbons on the surface prior to compounding. Fig. 2(b) and (c) illustrate two types of chemical modifications on the surface of fumed silica. A novel surface modification technique relies on the introduction of a carbon precursor during flame synthesis [42]. Kammler et al. [43] synthesized carbon-coated silica using a commercial hydrogen-air burner, by oxidation of hexamethyldisiloxane (HMDSO). It was found that by increasing the production rate and lowering the hydrogen concentration in the flame at a constant air-flow, nano-aggregates of carbon-coated silica could be produced with varying surface carbon content [43]. Kammler et al. [43] showed that the silica precursor rapidly reacts to SiO_2 nanoparticles followed by surface condensation of a graphitic carbon layer, Fig. 2(c).

1.2. Assessing binary interactions and filler dispersion

The physical properties of silica-filler/polymer nanocomposites depend on the colloidal structure of the particles. During flame synthesis, the aggregate structure that extends from a few nanometers to about a micron result directly from coalescence of unstable silica nanodroplets which form in the reaction zone of the flame. Further downstream, at lower temperatures, solid, stable primary particles emerge that continue to collide and fuse into fractal aggregates. These aggregates can also collide to form micron-scale agglomerates. This structural hierarchy is preserved even after high shear mixing with a polymer.

Combined small-angle (SAXS) and ultra-small angle (USAXS) X-ray scattering are useful to characterize hierarchical structures spanning multiple length scales. The scattered intensity, $I(q)$, from a binary nanocomposite is $I_{total}(q) - I_{back}(q) = \phi V <\Delta\rho>^2 P(q)S(q)$, where $I_{back}(q)$ is the scattered intensity from the isolated polymer matrix, which is subtracted before extracting structural information for the filler. Here, q is the momentum transfer or reciprocal space vector with units of inverse length. $<\Delta\rho>^2$ is the scattering contrast, or the electron density difference squared between the filler and the matrix. V represents the particle volume, $\phi = nV/V_{total}$ is the filler volume fraction, and n/V_{total} is the number density of particles. The structural details of the filler are determined from the form factor, $P(q)$, while the interparticle structure

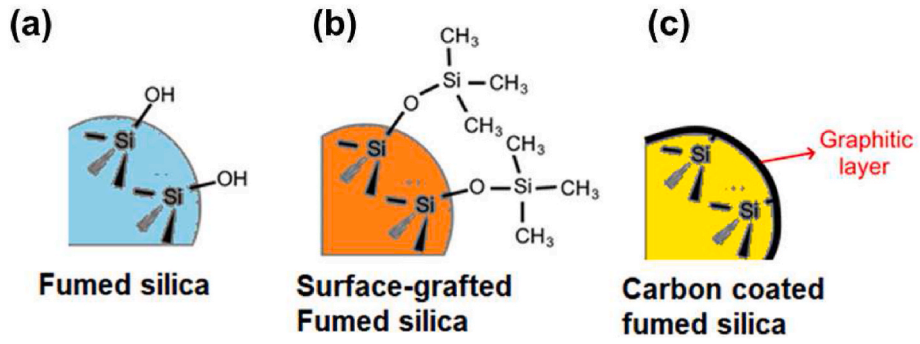

Fig. 2. Illustrations of the different chemical species on the surface of silica. (a) Isolated silanol groups on as-produced silica. (b) Hexamethyldisilazane treated silica. (c) Carbon/soot coated silica.

factor, $S(q)$, describes the correlation of aggregates [19]. Note that when the filler is present in dilute concentrations, i.e., $\phi = \phi_0$, $S(q) = 1$ and the form factor can be determined directly from the scattered intensity. Although $P(q)$ for simple shapes such as spheres is well known, industrial and commercially relevant fillers are far from perfect. The form factor for these complex multi-level hierarchical structures spanning various length scales can be described using the Unified scattering function [44–46],

$$I_0(q)/\phi_0 = \sum_{i=1}^{n}\left[\left(G_{i,0}/\phi_0\right)\exp\left(-q^2R_{g,i}^2/3\right) + \left(b_{i,0}/\phi_0\right)\left(q_i^*\right)^{-P_i}\exp\left(-q^2R_{g,i-1}^2/3\right)\right]$$

$$q_i^* = q\ /\ \mathrm{erf}\left(k\,qR_{g,i}/\sqrt{6}\right)^3 \tag{1}$$

In eq. (1), $I_0(q)/\phi_0$ is the reduced scattering intensity. i represents the index for the structural level such that 1 represents the smallest structural level, the primary particles. q_i* is a reduced parameter which describes, the transition between the power law and Guinier regimes within a structural level [45]. G_i is the Guinier pre-factor proportional to the number density of the particles and $<\Delta\rho>^2$, $R_{g,i}$ is the respective radius of gyration, whereas for the mass fractal aggregate level 2, $b_2 = G_2\,(C_{p,2}d_{min}/R_{g,2}^{df})\Gamma(d_f/2)$, here lower case "$b$" is used to distinguish from the molar second virial coefficient, "B_2". $C_{p,2}$ is the aggregate polydispersity factor, which measures the polydispersity of aggregate mass, $z = (G_2/G_1) + 1$ [47]. $\Gamma(x)$ is the gamma function, d_f is the mass fractal dimension while d_{min} is the minimum dimension or the mass fractal dimension of the weight average minimum path (short-circuit path) through a given structure. Each structural level also comprises a power-law region from which the power-law exponent, P_i, can be determined, describing the type of structure for that level, >3 solid structure with $k = 1$, <3 fractal or low-dimensional object with k ~1.06.

The interparticle structure factor, $S(q)$, becomes relevant above the local percolation threshold at commercial filler loading levels, $\phi >> \phi^*$, in the semi-dilute regime. In the absence of specific, Coulombic correlations in the case of neutral/surface modified particles, $S(q)$ smoothly rises to a plateau in q as a signature of mean-field behavior. The extent of structural screening, $\phi\nu$, can then be quantified through the mean-field random-phase approximation (RPA) [19,20] such that,

$$S(q) = \left(1 + \{\phi\nu(I_0(q)/\phi_0)\}\right)^{-1} \tag{2}$$

For silica with surface hydroxyls, local correlated structures emerge for filler concentrations above which particles interact within the Debye screening length. These correlations are characterized by a peak in the scattering profile associated with the presence of silanol groups on the surface [20]. The structure factor, using the Born-Green approximation for polydisperse correlations can be expressed by,

$$S(q) = \int_0^\infty P(\xi)\,[1 + p\theta(q,\xi)]^{-1}\mathrm{d}\xi \tag{3}$$

Here, $P(\xi)$ represents a log-normal distribution for correlation lengths with a geometric mean of $<\xi>$. $\theta(q,\xi) = 3\{\sin(q\xi) - (q\xi)\cos(q\xi)\}/(q\xi)^3$, represents the spherical amplitude function such that aggregates arrange in a spherical correlation shell. p is the volumetric packing factor that describes the degree of aggregate adherence to this domain shell, larger p the greater the adherence, 0 indicates no adherence for a random arrangement [19].

As $q \to 0$, $S(0) = (1 + \{\phi\nu\sum_{i=1}^{n}G_{i,0}/\phi_0\})^{-1}$ in the mean-field equation (eq. (2)). Additionally, $S(0) = (1+p)^{-1}$ in the specific interactions eq. (3). In this way mean-field behavior can be directly compared with specific interactions through, $\nu = p/(\phi\sum_{i=1}^{n}G_{i,0}/\phi_0)$ [19]. ν is related to the pseudo-second-order virial coefficient, B_2, as shown by Vogtt et al. [48] for equilibrium micellar systems and extended to non-equilibrium systems such as industrial nanocomposites by Jin et al. [49] such that,

$$B_2 = \nu\langle\Delta\rho\rangle^2 z^2\left(\pi d_p^3/6\right)^2/2 \tag{4}$$

Here, $d_p = 6(S/V)^{-1} = 6(\pi b_1/Q_1)^{-1}$ is the Sauter mean diameter of the primary particles which depends on the scattering invariant (Q_1) determined as the area under the Unified fit curve in an $q^2I_0(q)$ vs. q plot for level 1. Note that (S/V) represents the surface area to volume ratio of the primary particle. The units of B_2, are cm^3/aggregate. The molar second virial coefficient of osmotic pressure, B_2, quantifies colloidal interactions [50]. B_2 links the microscopic and the macroscopic properties of a thermodynamic system, such as the interaction potential and osmotic pressure. Miscibility in thermally dispersed systems such as colloidal dispersions can be quantified through the mass-concentration second virial coefficient. B_2 ~0 indicates the miscibility limit and $B_2 > 0$ indicates greater miscibility. In kinetically dispersed, immiscible polymer-filler systems, we have introduced a pseudo-second order virial coefficient from X-ray scattering in analogy to thermally dispersed colloids to quantitatively describe the dispersion of the filler aggregates in polymer melts with temperature replaced by accumulated strain [10,11,49], as opposed to traditional methods based on micrograph analysis [51–53], and simulations [54].

In the present study, carbon-coated fumed silicas with varying surface carbon content mixed with an SBR matrix were investigated. SBR was chosen since it is commonly used in automobile tire treads. Carbon coating was achieved by oxidation of hexamethyldisiloxane during flame-synthesis as detailed by Kammler et al. [43]. Flame-modified fumed silica with varying surface carbon content leads to a change in elastomer and filler interaction and filler dispersion quantified through the second virial coefficient determined from small-angle scattering. Additionally, an assessment was made of the impact of the surface carbon content and silanol content on tanδ measured under oscillatory shear.

2. Experimental

2.1. Sample preparation

Four grades of pyrogenic silica varying in surface carbon content (weight %), as shown in Fig. 3 (right), were prepared by flame synthesis [43]. A commercial grade of fumed silica, Aerosil® 200, with no surface carbon content and a specific surface area of 200 m^2/g, was provided by Evonik Corporation, 2 Turner Place, Piscataway, NJ 08854, USA. The specific surface areas of the modified fumed silica fillers shown in Fig. 3 (right) were determined by (Brunauer–Emmett–Teller) BET analysis [43] whereas the surface carbon content was ascertained through a mass spectrometer/carbon dioxide sensor connected to a thermogravimetric analysis (TGA) balance [55]. A schematic of the flame synthesis setup is shown in Fig. 3 whereas some details about the production of these modified silicas can be found in Table T1 in Appendix B in the Supplementary Information.

These flame-synthesized fumed silica grades were melt compounded with a commercially available SBR with 24 wt% vinyl (for the polybutadiene blocks) and 38 wt% styrene. This SBR had a Mooney viscosity (ML 1 + 4 at 100 °C) of 80 M U. Mixing of nanofiller and polymer was conducted in a 50 g Banbury (Brabender) mixer. SBR was loaded while the mixing screws ran at 30 rpm at a temperature of 130 (±5) °C followed by addition of the antioxidant, [N-(1,3-dimethylbutyl)-N′-phenyl-1,4-phenylenediamine] or 6PPD (TCI America). Finally, the modified silica was added to the mixer and the rotor speed set to $N = 60$ rpm after closing the ram. The polymer-filler mixture was masticated for $t = 20$ min. following which the mixed melt was dispensed. Each grade of fumed silica was mixed in SBR at two loading levels viz. 1 wt% (dilute) and ~16 wt% (semi-dilute) following McGlasson et al. [11,20]. A Couette flow was considered to estimate the accumulated strain in the Banbury mixer geometry such that $\gamma = \left(\frac{4\pi\,(D_W/D_R)^{2/n}}{n\{(D_W/D_R)^{2/n}-1\}}\right)Nt$ following Bousmina et al. [56]. The wall to rotor ratio, D_W/D_R, was approximately 1.14 for the Banbury mixer used in this study, whereas the power-law index, n, for SBR is ~1 [57]. This resulted in γ ~64,300.

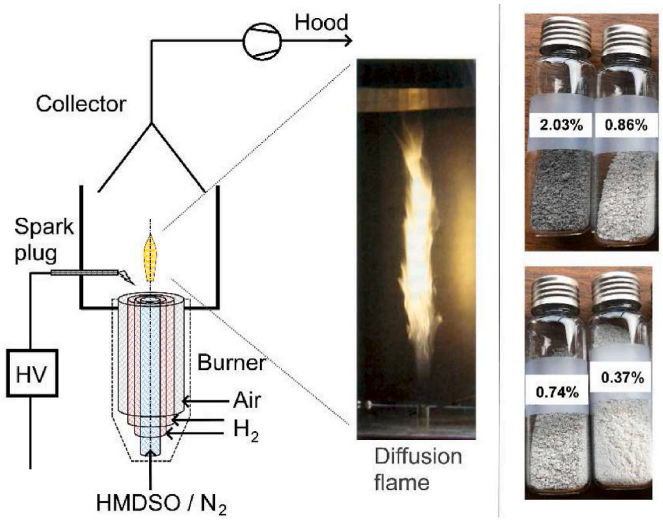

Fig. 3. (left) Schematic of the flame synthesis setup used to generate carbon/soot coated silica particles with an exploded view of the actual flame wherein the pristine silica is coated with carbon downstream (yellow flame emission) Reprinted with minor changes from AIChE Journal, Vol 47, H.K. Kammler, R. Mueller, O. Senn, S.E. Pratsinis, Synthesis of silica-carbon particles in a turbulent H2-air flame aerosol reactor, Pages 1533–1543, Copyright © 2001 American Institute of Chemical Engineers (AIChE) with permission from John Wiley and Sons [43]; (right) Flame synthesized particles with varying surface carbon content used in this study. The surface carbon content determined via elemental analysis is mentioned on each fumed silica vial. (For interpretation of the references to colour in this figure legend, the reader is referred to the Web version of this article.)

2.2. Elemental analysis

Elemental analysis was performed on a PerkinElmer 2400 II analyzer (Micro Analysis Inc., 2038 Telegraph Rd, Wilmington DE 19808) to determine the carbon content coated on the surface of flame-synthesized pyrogenic silica. About 10 mg of the silica powders were weighed and combusted in a ceramic crucible at 925 °C in the presence of pure oxygen (99.8%). The quantity of effused carbon dioxide was measured by thermal conductivity detectors, and the detected amount relative to the initial sample weight was expressed as the percentage of carbon. Note that prior to analysis, the samples were dried at 125 °C for 30 min to remove moisture. In the present study, the surface carbon content varied from ~0.3 to 2 wt%. Commercially available fumed silica, Aerosol® 200, contains no surface carbon (0 wt%).

2.3. Fourier transform infrared spectroscopy (FTIR)

FTIR spectra of the flame-modified silica powders were obtained on a Nicolet 6700 FT-IR spectrometer operated in attenuated total reflection mode (ATR) mode using a diamond crystal. For each IR spectrum, the measured transmittance was converted to absorbance and baseline corrected using the OMNIC software. For a quantitative estimate of the surface silanol content, the ratio of areas under the O-H and Si-O peaks was considered following Rishi et al. [19].

2.4. Ultra small-angle X-ray scattering (USAXS)

For small-angle scattering measurements, the melt-mixed nanocomposites were pressed into standard flat face metal washers so that a thickness of 1.2 mm was maintained. These washers were clamped and subsequently baked in an oven at 100 °C for 10 min. USAXS measurements were performed at the beamline 9-ID-C at the Advanced Photon Source (APS), Argonne National Laboratory. This instrument is operated by Jan Ilavsky [58]. USAXS data was recorded over four decades in size, $0.0001\ Å^{-1} < q < 1\ Å^{-1}$ so that the multi-hierarchical structure can be resolved. USAXS measurements were made at three distinct positions on the sample, and the average values for the fit and derived parameters are reported. The scattered intensity from the different nanocomposites was reduced, the scattered intensity from the polymer subtracted and subsequently desmeared to account for slit smearing effects through the Irena package of 9-ID-C at APS using Igor Pro® [59]. The contrast between the silica particles and the polymer, $<\Delta\rho>^2$, was computed via the scattering contrast calculator available in the Irena package of 9-ID-C at APS using Igor Pro® [59].

2.5. Dynamic rheology under oscillatory shear

The dynamic viscoelastic response of the nanocomposites was measured on a Discovery HR-2 rheometer by T.A. Instruments with parallel plate geometry. 3 mm thick sample disks (20 mm diameter) pressed between heated platens at 125 °C for 3 min were subjected to isothermal oscillatory shear at a fixed strain amplitude of 0.1% over four decades in frequency. Dynamic frequency sweeps at 25 °C, 75 °C and 125 °C using a standard steel Peltier plate for thermal control were used to construct master curves at $T_{ref} = 25$ °C. The experimental shift factors were then used to determine the constants in the William-Landel-Ferry (WLF) equation. Herein we assume that the time-temperature superposition is valid. Alternatively, temperature sweeps at specific frequencies can also be measured.

3. Results

3.1. Surface carbon and silanol content on silica nanoparticles

Table 1 shows the weight percent carbon determined from elemental analysis of the modified fumed silica powders. This weight percent was normalized by the surface area to mass ratio to determine the weight of carbon deposition on the surface per nm^2. Normalizing by the $(S/V\rho)^{-1}$ accounts for variations in the particle size, d_p, from USAXS analysis where ρ is the density of particulate silica, 2.2 g/cm^3. The S/V ratio can be directly computed from the Unified Fit results as described later. A higher surface carbon content (g/nm^2) indicates more hydrophobicity and less polar filler surfaces. The number of surface carbon monolayers, tabulated in Table 1, indicate the extent of carbon on the silica surface. The number of carbon atoms/Å^2 is computed by normalizing the surface carbon content in g/nm^2 with the molar mass of carbon.

In the flame, silica forms first then carbon nucleates on its surface, Fig. 4(a). Fig. 4(b) contrasts the wt% surface carbon from elemental analysis with the TGA measurements. The estimates from elemental analysis were consistently higher than the TGA estimates (refer Table T1 in Appendix B in the Supplementary Information), although the trend in both measurements was consistent. It is possible that the TGA measurement is lower because some carbon may be pyrolyzed at a higher temperature and over a broad temperature range where it is not easily measured. For this reason, the elemental analysis values are more accurate.

3.2. Hierarchical structure of silica nanoparticles mixed in SBR

Fig. 5 shows a log-log plot of the reduced scattered intensity, $I_0(q)/\phi_0$, versus the scattering vector, q, for the dilute ($\phi_0 \approx 0.0043$) modified fumed silica in SBR with a surface carbon content of 0.74 wt%. The $I_0(q)/\phi_0$ vs. q plots for all other dilute flame-synthesized fumed silica nanocomposites are shown in Appendix B in the Supplementary Information, Figs. S2–S5. In Fig. 5 and Figs. S2–S5, several structural levels can be distinguished, each with a distinct Guinier knee and a corresponding power-law regime. Since the abscissa represents the reciprocal space, large q or the region to the right of the plot is associated with the smallest structures. Details of these hierarchical multi-level structures can be ascertained through the Unified Fit [44,45] (solid line in the figures). In Fig. 5, the fit region is depicted by vertical lines on the plot in the range $0.0006\ \text{Å}^{-1} < q < 0.04\ \text{Å}^{-1}$, the Unified curve is extended beyond the fit range for clarity. For $q < 0.0006\ \text{Å}^{-1}$, a power-law slope between −3 and −4 is associated with surface scattering from agglomerates (level 3). Note that this region was not included in the fit. For $0.0006\ \text{Å}^{-1} < q < 0.04\ \text{Å}^{-1}$, two distinct power-law slopes are observed.

Table 1
Surface carbon content, N_C, surface silanol content, N_{OH}, and the number of carbon monolayers on the surface of the flame-modified silica nanoparticles.

Surface carbon[a] (wt%)	Carbon content[b] (× 10^{-21} g/nm^2)	Carbon content, N_C (#/nm^2)	# of Carbon monolayers (per Å^2)	Silanol content, N_{OH}[c] (#/nm^2)
0[d]	0	0	0	2.80[e]
0.37	2.2	111	1	3.73
0.74	4.4	218	2	3.35
0.86	6.2	310	3	4.66
2.03	22.6	1136	11	3.17

[a] From elemental analysis.
[b] Surface carbon in wt% normalized by $S/V\rho$ computed from the scattering results.
[c] From FTIR peak area ratio in Fig. S1 in Appendix A in the Supplementary Information.
[d] Commercial fumed silica Aerosil® 200.
[e] From Mueller et al. [55].

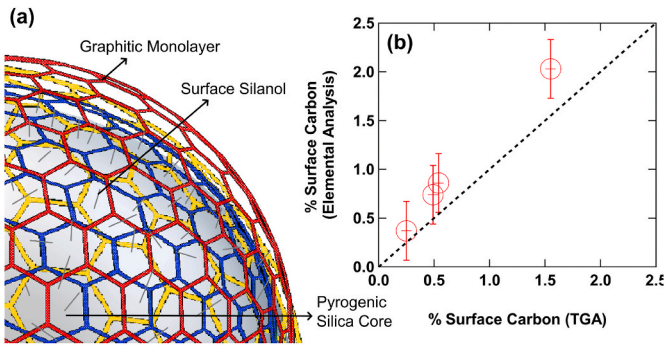

Fig. 4. (a) A cartoon of the modified fumed silica surface depicting the surface silanols and the coated carbon/graphitic monolayers. (b) Percentage of surface carbon content from elemental analysis compared with the carbon content from TGA measurements (listed in Table T1 in Appendix A in the Supplementary Information) for the modified fumed silica powders.

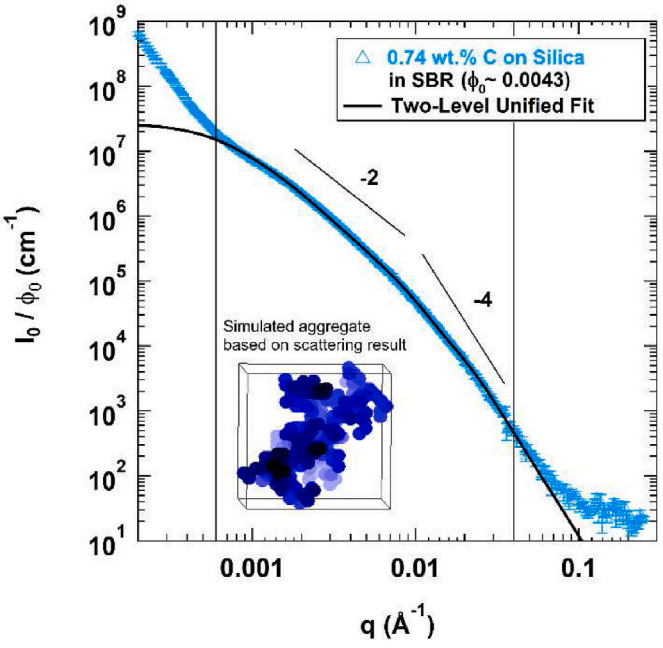

Fig. 5. Log-log plot of the reduced scattered intensity, $I_0(q)/\phi_0$, vs. q (scattering vector) for the flame-synthesized silica nanofiller coated with 0.74 wt% of carbon in the SBR polymer matrix at a dilute concentration, $\phi_0 \approx 0.0043$. The inset shows a simulated aggregate structure [60] whose topology agrees with the aggregate topological parameters based on the Unified Fit [44,45], eq. (1). The reduced scattered intensity, $I_0(q)/\phi_0$, vs. q plots for the remaining silicas coated with 0 wt% (Aerosil 200), 0.37 wt%, 0.86 wt% and 2.03 wt% carbon shown in Figs. S2, S3, S4, and S5, respectively in Appendix B in the Supplementary Information.

The slope of −4, at highest-q, indicates that the smallest structures (primary particles/level 1) are smooth, three-dimensional objects whereas, the slope of about −2.2 at lower q indicates that the filler aggregates (level 2) are mass-fractals with mass-fractal dimension, $d_f \approx 2.2$. Between the power-law slopes for each level, distinct Guinier knee regions yield the radius of gyration, contrast, and composition of each structural level ($R_{g,1}$ and $R_{g,2}$).

The fit parameters are tabulated in Table T2 in Appendix B in the Supplementary Information. These fit parameters were used to characterize the filler aggregate topology, the primary particle size (d_p), and the number of primary particles per aggregate (z), as shown in Table 2 [44–46]. The weight average number of primary particles within an aggregate, $z = (G_2/G_1) + 1$, was determine from the Guinier pre-factors

Table 2
Primary particle and aggregate topological parameters computed from the Unified fits to the dilute scattering curves for various carbon-coated fumed silicas in the SBR matrix.

Surface carbon content (wt%)	Primary particles			Aggregates				
	d_p (nm)	PDI	z	R_{eted} (nm)	d_f	d_{min}	c	ϕ_{br}
0	11 (±0.5)	9 (±1)	560 (±80)	150 (±10)	2.5 (±0.03)	2.1 (±0.1)	1.2 (±0.06)	0.56 (±0.02)
0.37	16.4 (±0.1)	9 (±0.4)	310 (±30)	193 (±9)	2.3 (±0.01)	1.6 (±0.04)	1.5 (±0.03)	0.85 (±0.01)
0.74	16 (±1)	11 (±0.3)	280 (±50)	210 (±10)	2.2 (±0.02)	1.3 (±0.02)	1.7 (±0.04)	0.90 (±0.02)
0.86	20 (±1)	12 (±0.5)	190 (±20)	240 (±20)	2.1 (±0.03)	1.2 (±0.03)	1.8 (±0.03)	0.90 (±0.01)
2.03	30 (±2)	10 (±1)	120 (±3)	360 (±50)	1.9 (±0.06)	1.1 (±0.08)	1.8 (±0.07)	0.88 (±0.01)

for the two structural levels. $R_{eted} = d_p\ (z)^{1/df}$, is the aggregate end-to-end distance where $d_f = -P_2$ (mass-fractal dimension of the aggregate). The polydispersity in primary particle size was obtained from $PDI = (G_1 R_{g,1}^4)/(1.62 b_1)$ [48,61–63]. Other parameters that describe the aggregate topology were also derived from the Unified results and are listed in Table 2 as d_{min}, c and ϕ_{br} which represent the dimension of an average short-circuit path (convolution), the aggregate connectivity dimension (topology) and the average branch fraction per aggregate, respectively [60]. The degree of aggregation, z, was used as an input parameter for a simulation code from Mulderig et al. [60], to generate an aggregate structure that matches the Unified fit parameters from USAXS shown in Fig. 5 (inset) using the Irena software from 9-ID-C APS [59]. The aggregate structure is highly branched as indicated by the large ϕ_{br} and c approaching d_f in Table 2. Aggregate structures generated through this method have been demonstrated to qualitatively agree with TEM micrographs in our previous works [19,28,60].

Fig. 6(a) compares the specific surface area obtained from scattering to BET gas adsorption (refer Table T1 in Appendix A in the Supplementary Information). A larger specific surface area from scattering is expected since scattering measures both open and closed pores in the nanofillers while gas adsorption is limited to open pores only. Fig. 6(b) compares the degree of aggregation of primary particles with the Sauter mean diameter of the primary particles determined from scattering. It is observed that the degree of aggregation increases with $z = K''\{(1/d_p) - (1/d_{p,max})\}$. The Sauter mean diameter, d_p, is the equivalent spherical size obtained from the S/V ratio, $d_p = 6V/S$. The observed behavior indicates that the degree of aggregation is proportional to the surface to volume ratio of the nanoparticles and that there is a maximum size beyond which aggregation does not occur, $d_{p,max}$ ~43 nm. For example, carbon black conforming to ASTM N330 grade with a d_p ~42 nm showed an exceptionally low degree of aggregation of ~7 primary particles [10]. The slope $K'' = 8$ (±1) μm indicating that there is a strong and predictable dependence of z on d_p. The most important parameters in determining the primary particle size are flame temperature and particle residence time. Thus, one would expect K'' to be a function of both flame temperature as well as the particle residence time [43]. Since d_p and z in Fig. 6(b) were estimated after mixing the fumed silica powders, K'' could additionally depend on the total accumulated strain during the high shear mixing process.

3.3. Structural emergence with varying surface carbon content on silica

Fig. 7(a) and (b) show the reduced scattering intensity, $I(q)/\phi$, as a function of the reciprocal lattice vector, q, under semi-dilute filler concentration for the fumed silica nanofillers with 0 wt% and 2.74 wt% surface carbon, respectively. Similar plots for the 0.37 wt%, 0.74 wt%, and 0.86 wt% are shown in Figs. S6, S7, and S8, respectively in Appendix B in the Supplementary Information. The dilute reduced scattering intensity plots, $I_0(q)/\phi_0$ vs. q are shown along with the structure factor, $S(q)$, which is the ratio of the reduced scattering intensities under semi-dilute and dilute loading levels, $S(q) = I(q)\phi_0/I_0(q)\phi$. The $S(q)$ values can be read from the right ordinate on all the plots. The overlap concentration for fractal silica aggregates, in analogy to polymer solutions, is the point where local percolation on the nanoscale commences. Nanofiller concentrations above overlap, are termed semi-dilute. In Fig. 7(a) and (b), both $I_0(q)/\phi_0$ and $I(q)/\phi$ overlay in the high-q region, thereby affirming that the primary particle structure remains unchanged under semi-dilute concentrations. Consequently, in this region $S(q) = 1$. However, in the aggregate region at lower-q, a distinct broad peak appears followed by a drop in $S(q)$ in Fig. 7(a) and Figs. S6–S8 for the lower surface carbon contents. The appearance of peaks in this q range indicates the emergence of correlated aggregates due to silanol interactions. $S(q)$ in Fig. 7(a) and S6-S8 were fit using eq. (3). On the contrary, in Fig. 7(b) this correlation peak disappears completely indicating that specific surface interactions due to the silanol groups do not lead to aggregate correlations when the carbon coating on the silica surface increases or the number of carbon monolayers increase. $S(q)$ in Fig. 7(b) was fit using the mean-field model in eq. (2). The mean-field model involves a random distribution of overlapping aggregates. Thus, the locally percolated emergent structure changes from correlated aggregates to a randomly distributed aggregate network with increasing surface carbon content at similar nano-silica loading levels (ϕ ~0.09) for all nanocomposite systems studied here.

At low-q, below 0.001 Å^{-1}, in Fig. 7(a) and S6-S8, a steep slope is seen in the semi-dilute $I(q)/\phi$ curves in the presence of correlations at low carbon content which is associated with agglomerates of aggregates.

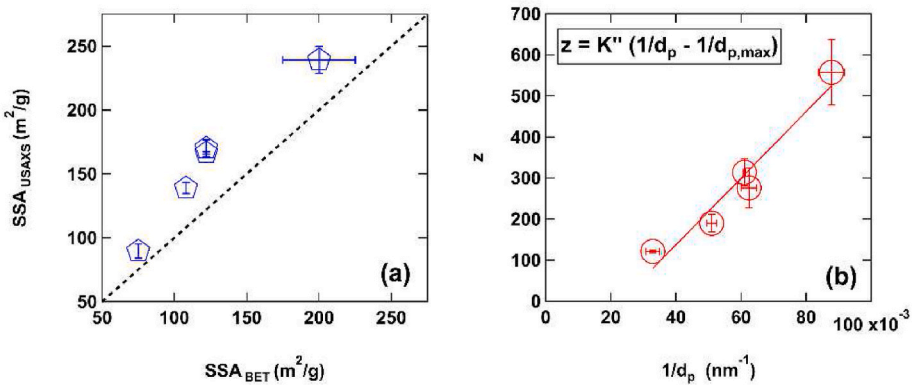

Fig. 6. (a) A comparison of the specific surface area of the flame-synthesized carbon-coated silica nanofillers from USAXS and BET gas adsorption. Note that the BET specific surface area for the commercial fumed silica grade was obtained as the average value of the range specified in the product specifications [64], whereas the values for the synthesized carbon-coated silica are listed in Table T1 in Appendix A in the Supplementary Information. The specific surface area from USAXS is larger since the X-rays can measure both open and closed pores. (b) A plot showing the dependence of the degree of aggregation on the silica nanofiller primary particle size. The plot indicates that as the primary particle size reduces, the degree of aggregation increases proportional to the specific surface area.

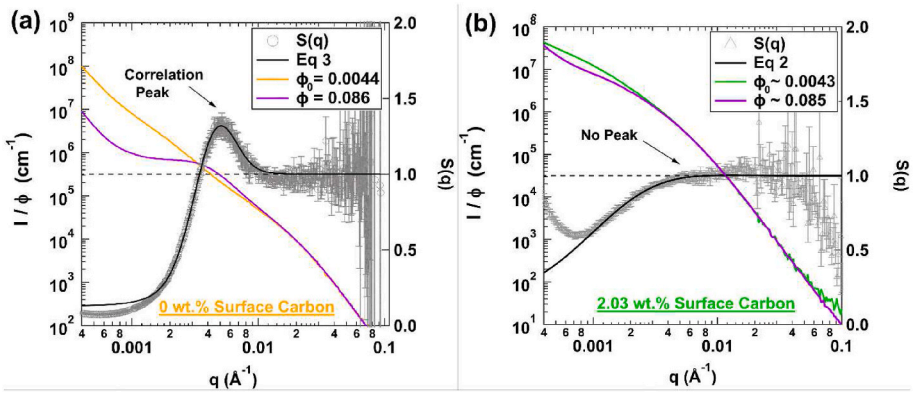

Fig. 7. Log-log plot of the reduced scattered intensities, $I_o(q)/\phi_0$ and $I(q)/\phi$ (read from the left ordinate) and the inter-particle structure factor, $S(q)$ (read from the right ordinate) as a function of the scattering vector q for pristine, (a) 0 wt%, and modified silica nanofillers with (b) 2.03 wt% surface carbon content in SBR. The plots for 0.37 wt%, 0.74 wt%, and 0.86 wt% surface carbons are shown in Appendix B in the Supplementary Information. Note that ϕ_0 and ϕ represent the dilute and semi-dilute filler concentrations, respectively, as listed in the plots. For (a), a broad peak at intermediate q in the $S(q)$ plots, indicates the emergence of correlated aggregates. For (b), an absence of a peak in the aggregate region at intermediate q in the $S(q)$ plots indicates that the nano-aggregates overlap and are randomly distributed.

For large carbon content in Fig. 7(b) with no aggregate correlations this steep slope is below −3 indicating the formation of an emergent filler network whose mass-fractal dimension is the negative of the steep slope in the log-log plot. The emergence of agglomerates is not accounted for in either eq. (2) or eq. (3) so the fit underestimates the measured $S(q)$ in this region in all cases except for Fig. 7(a) where the dilute sample shows stronger aggregation compared to the semi-dilute sample leading to an overestimation of eq. (3) compared to the measured $S(q)$ in the low-q region for this sample, however, eq. (3) agrees well even in this low-q region indicating that there is a low-degree of aggregation and filler network formation in the absence of carbon coating.

It has been previously shown that the transition from random, mean-field interactions to correlated specific interactions occurs at a critical ordering concentration (COC) above ϕ^* ~0.05 for silica nanofillers with predominantly hydrophilic surface groups [19]. This COC depends on the dielectric constant of the polymer matrix [19]. In the present study, ϕ^* ~0.09 for all silica grades and one might expect that at higher loadings the silica nanoaggregates would correlate. However, an increase in the surface carbon content in these nanofillers at the same silica loading can disrupt this ordering phenomenon. The emergence of these starkly different interaction types can be reconciled by considering the number of carbon monolayers in Table 1. The thickness of a graphene monolayer is approximately 3.4 Å to 3.6 Å [65]. In contrast, the atomic radii of O, H and Si are 0.5 Å, 0.25 Å and 1.1 Å respectively, the Si-O bond length is ~1.56 Å [66] and the O-H bond length is 0.96 Å [67]. This would result in an overall thickness of ~4.4 Å for a surface normal silanol. Considering that the silanols are statistically distributed over the silica surface and that the slight negative charge of surface silanols acts over some distance between silica aggregates, one would expect about 2–3 monolayers of carbon on the surface to be able to shield the silanol charge. This conjecture is supported by the observed structural emergence in Fig. 7 and S6-S8, where correlations are absent in Fig. 7(b) when the number of carbon monolayers is calculated to be 11, versus 3 monolayers for Figs. S8 and 2 for Fig. S7 which show weak correlations.

3.4. Assessment of nanofiller dispersion with varying surface carbon content

Table 3 lists the $S(q)$ fit parameters for the silica nanofillers mixed in the SBR matrix. Aggregates with more carbon monolayers can diminish the silanol charge repulsion. For fillers that have a lower number of carbon monolayers, specific interactions due to silanol charge repulsion dominate. The resulting correlated peak is characterized by an aggregate packing factor (p), the average mesh size, $<\xi>$, and the geometric deviation in the mesh size, σ. p is expected to lie between 0 and 5.92 for hard spheres (8 × 0.74 for closest packed spheres) [46]. Mass-fractal aggregates can pack more closely due to asymmetry and interpenetration leading to larger values of p [20]. The peak position from the structure factor fits in Fig. 7(a) and S6-S8 at the specified semi-dilute filler concentration is related to the correlation distance/mesh size, $<\xi>$, averaged over all domains of varying accumulated strain as discussed in Refs. [19,20]. Note that no distinct domains are needed in the mean-field approach in 7(b) since all binary interactions are averaged.

Reference [11] introduced the use of an analogy between the accumulated strain, γ, in kinetically mixed systems and the temperature, k_B, in thermally dispersed systems. For thermally dispersed systems the van der Waals (vdW) equation can be used to express $B_2(T)$ in terms of the excluded volume, b, and the enthalpic interaction, a, $B_2(T) = b - a/k_BT$. For kinetically mixed systems, $B_2 = b^* - a^*/\gamma$. The excluded volume, b^*, can be calculated from the dilute scattering curve. For polymer nanocomposites, $a^* = \gamma\,(b^* - B_2)$. Dispersion in melt compounded polymer nanocomposites is governed by the accumulated strain as opposed to temperature. The accumulated strain is governed by the shear rate, mixing duration and the mixer geometry [11]. b^* is the excluded volume per aggregate, determined from the computed values of d_p and z in Table 2 such that, $b^* = 4z\pi\,(d_{p,app}^3/6)$ per aggregate [10,19]. For carbon black nanofillers, the ratio of the excluded volume to the hard-sphere excluded volume, $V_{ex}^{HS} = 4z\pi\,(d_p^3/6)$, was ~2 [10], whereas, this ratio increased to ~5 [11] for carbon-coated silica. Here, the apparent

Table 3
Fit parameters for semi-dilute (ϕ ~0.09) nanocomposite fillers in SBR. a^* is the attractive enthalpy from the van der Waals analysis.

Surface carbon content (wt%)	ϕ	p	σ	ξ or $<\xi>$ (nm)	ν (× 10^{-6} cm) *	B_2 (× 10^{-15} cm^3/agg.)	a^* (× 10^{-10} cm^3/agg)
Specific interactions							
0	0.086 (±0.005)	6.8 (±0.2)	0.35 (±0.02)	133 (±1)	3.4 (±1)	3.0 (±0.3)	1.8 (±0.6)
0.37	0.09 (±0.02)	4.3 (±0.6)	0.53 (±0.05)	210 (±13)	1.4 (±0.5)	3.5 (±1)	4 (±1)
0.74	0.088 (±0.003)	4.7 (±0.6)	0.69 (±0.03)	350 (±30)	2.6 (±0.9)	4 (±2)	2.4 (±2)
0.86	0.078 (±0.001)	5.1 (±0.7)	0.47 (±0.02)	210 (±4)	2.4 (±0.4)	6 (±2)	2.5 (±2)
Mean-field interactions							
2.03	0.085 (±0.005)	–	–	700 (±20)	0.8 (±0.03)	12 (±5)	7.7 (±3)

* The screening parameter, ν, for the mean-field model was determined by fitting $S(q)$ to eq. (2) whereas, ν for the specific interaction model was computed by fitting $S(q)$ to eq. (3) to obtain p and then using $\nu = p/(\phi \sum_{i=1}^{n} G_{i,0}/\phi_0)$.
** The pseudo-second virial coefficient, B_2, was determined using eq. (4).

particle diameter, $d_{p,app}$ ~$1.5d_p$ was used to account for the bound rubber layer [10]. Recent small-angle neutron scattering studies on fumed and precipitated silica with primary particle size ranging from 14 nm to 20 nm have shown that the statistical bound layer thickness ranges from 6.5 nm to 10.3 nm [68].

Fig. 8 shows the interaction potential a^*, listed in Table 3, as a function of the surface density of carbon, N_C (# per nm^2) and silanols N_{OH} (# per nm^2), listed in Table 1, using a linear scaling law, $a^* = A' + K'_C N_C + K'_{OH} N_{OH}$. a^* is an attractive potential between aggregates that drives clustering like the vdW 'a' for real gases. A negative value indicates an effective repulsion between aggregates. Here, A' has a large positive value indicating that in the absence of hydroxyls and carbon the particles are attractive. K'_C and K'_{OH} reflect the relative impact of the surface carbons and silanols. K'_{OH} is negative indicating that the addition of silanols increase the repulsion between aggregates due to Coulombic interactions compared to bare silica. K'_C is positive indicating that the addition of surface carbon increases the attraction between aggregates compared to bare silica. It should be noted that independent account of the impact of the coupling of carbon coating on silanol groups (the cross correlation) has not been made so this impact is included in K'_C. There are one to two orders more carbon than silanols, Table 1, and K'_C is about two orders smaller than K'_{OH} which indicates that the impact of carbon and silanol with the experimental surface number densities is approximately equivalent though opposite in terms of attraction and repulsion between the aggregates. At $a^* = A'$, the two opposing effects of surface hydroxyls and surface carbon is nullified. For this condition, $K'_C N_C + K'_{OH} N_{OH} = 0$ such that N_C/N_{OH} ~70 based on the fit results shown in Fig. 8. For surface hydroxyl density (N_{OH}) ranging between ~3 and ~5 in this study (refer Table 1), one would expect N_C to range between 200 and 350, respectively which is about 2–3 monolayers. This is consistent with the estimated monolayers that would shield the silanol charge in the previous section.

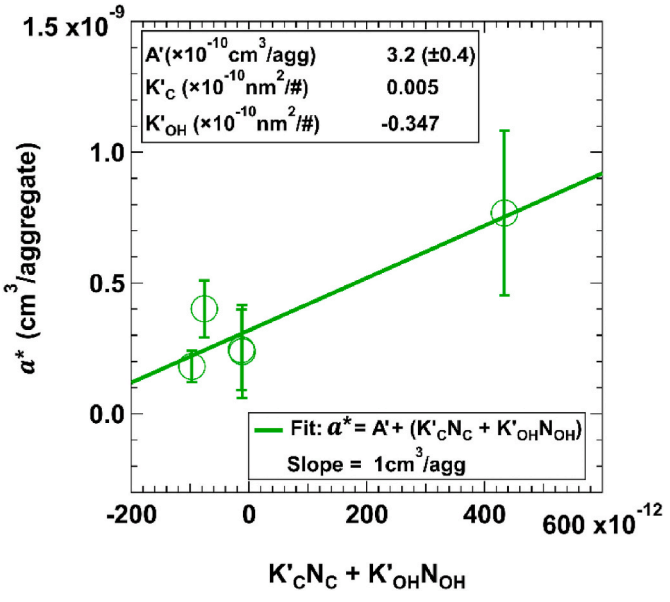

Fig. 8. Plot of the particle interaction parameter, a^*, expressed in cm^3/aggregate as a function of the linear sum of the surface carbon content (N_C) and surface hydroxyl content (N_{OH}) weighted differently. N_C and N_{OH} are reported in Table 1 a^* is an attractive potential so negative values indicate relative repulsion between aggregates that increases with surface carbon content. That is, surface carbon enhances aggregate/polymer attraction relative to aggregate/aggregate attraction. The fit parameters, A', K'_C, and K'_{OH} were obtained through least squares minimization.

3.5. Dynamic response of silica in SBR with varying surface carbon content

The dynamic response of surface-modified silica nanofillers in the SBR matrix was examined using small strain amplitude oscillatory rheology at $T_{ref} = 25\,^{\circ}C$. The storage modulus (G') master curves for nanocomposites containing 0 wt%, 0.37 wt%, 0.74 wt%, 0.86 wt% and 2.03 wt% surface carbon silica at semi-dilute silica concentration (ϕ ~0.09) in Figs. S10–S14 were compared to the neat SBR (G_0') master curve (Fig. S9) scaled by the hydrodynamic reinforcement factor in Appendix C in the Supplementary Information. The hydrodynamic reinforcement factor was determined from Medalia's modification to the Einstein-Guth model for moduli enhancement due to addition of particles [69–73]. $H_{shift} = G'/G_0' = 1 + 2.5\phi_{eff} + 14.1\phi_{eff}^2$, where the quadratic term accounts for the fractal nature of the aggregate, and the effective volume fraction, ϕ_{eff}, accounts for the apparent increase in volume fraction due to rubber occlusion. In Figs. S10–S14 in Appendix C in the Supplementary Information, the high frequency region where G' and $H_{shift}G_0'$ overlap was fit using a power law, while the low frequency region for G' was fit to another power-law following Rishi et al. [28]. The intersection of the two power laws at $\omega^* = 1/\tau^*$ is related to the mesh size, ξ, determined from scattering, Table 3, through the static aggregate connectivity dimension or the spectral dimension, c, listed in Table 2 as shown in Fig. S15 in Appendix C in the Supplementary Information. Fig. S16 in Appendix C in the Supplementary Information compares the complex viscosity, η^*, for the nanocomposites containing 0 wt%, 0.37 wt %, 0.74 wt%, 0.86 wt% and 2.03 wt% surface carbon silica at semi-dilute silica concentration (ϕ ~0.09) with that of the neat SBR at a reference temperature of 25 °C. Over the extended frequency, η^* of the samples with higher surface carbon content are closer to the neat SBR while η^* in the absence of surface carbon is the highest. This trend supports the observed filler dispersion (B_2) which increases with increasing surface carbon as shown in Table 3. A lower viscosity due to increased polymer-filler compatibility would positively impact dispersion since aggregate transport is difficult in more viscous media. To achieve better-wet grip and rolling resistance, tire compounders use both carbon black that increases wet grip, and silica that lowers the rolling resistance [74,75]. A lower rolling resistance is characterized by a reduced tanδ or an increased storage modulus at 60 °C and 1 Hz whereas, better-wet grip is achieved by larger tanδ values or an increase in the energy loss at 0 °C and 1 Hz. Instead of 1 Hz, we use the tanδ at $T_{ref} = 25\,^{\circ}C$ associated with the emergent filler structure at ω^* to obtain tanδ at 0 °C and 60 °C as shown in Fig. S17 in Appendix C in the Supplementary Information. We assume that the tanδ at these two temperatures is influenced by the surface composition of the silica in a linear manner, $\tan\delta = A + K_C N_C + K_{OH} N_{OH}$, Fig. 9. The base value of tanδ in the absence of these surface groups is A which is modified by a linear sum of the carbon, K_C, and hydroxyl, K_{OH} groups weighted differently. The positive sign to the weighting factor, K_C indicates that carbon enhances tanδ while a negative sign for K_{OH} indicates that hydroxyls deplete tanδ.

tanδ for rolling resistance has about 8 times the dependence on N_C as tanδ for wet grip. Similarly, tanδ for rolling resistance is about 8 times the dependence for N_{OH} compared to wet grip. With the concept of increasing tanδ for wet grip while reducing tanδ for rolling resistance we can sum the two equations under the assumption that a drop in tanδ for rolling resistance and a drop for wet grip can be considered equivalent in value, then one should seek to increase N_{OH} and drop N_C, the two cancelling each other's effect at about $N_C/N_{OH} = 500$. For the samples studied here the closest to this ratio is for the highest carbon content where highest carbon content $N_C/N_{OH} = 358$.

4. Conclusion

The effects of surface carbon content on flame-modified pyrogenic silica fillers on dispersion, particle interactions and rheological properties in styrene butadiene rubber was studied. Structural characterization

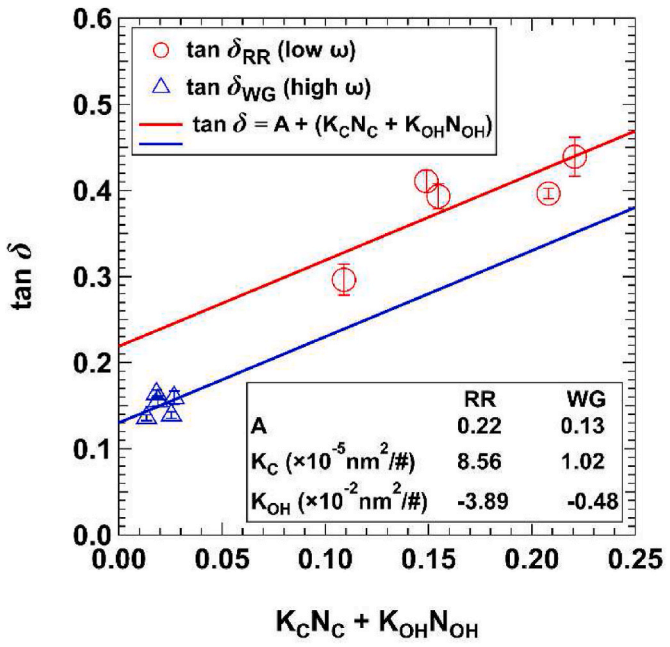

Fig. 9. tanδ for rolling resistance and wet grip as a function of the surface content of the hydroxyl groups (N_{OH}) and carbon coating (N_C) weighted differently. The fit parameters, A, K_C, and K_{OH} were obtained through least squares minimization.

revealed that these silica filler aggregates were mass fractals, such that their degree of aggregation, z, was inversely related to the primary particle size, d_p. X-ray scattering results for untreated silica and silica with low surface carbon contents showed a characteristic peak indicative of structural correlations in the emergent meso-scale structures. This emergence was attributed to the specific interactions due to the surface silanol groups. For the fillers that contain a greater carbon surface coverage, typically more than 2–3 monolayers, this charge repulsion is shielded resulting a random dispersion of filler aggregates. The extent of dispersion in this case was assessed through a mean-field interaction model. This transition from specific to mean-field interactions with varying surface carbon content on silica indicates that the emergent network structures can be tuned as demonstrated by the estimation of the binary interaction potential, a^* based on a modified van der Waals approach. a^* is related to the surface carbon (N_C) and surface hydroxyl (N_{OH}) densities such that a^* increases as N_C increases and decreases with N_{OH}, indicating that filler dispersion can be tuned by varying the surface carbon content. The rolling resistance and wet grip associated with the emergent structures in the nanocomposites were found to depend on the surface densities of both carbon (N_C) and hydroxyls (N_{OH}) as well. It is concluded that to maximize wet grip and minimize rolling resistance, surface modified pyrogenic silica fillers with optimal surface carbon content can be mixed in styrene butadiene rubber.

Notes

The authors declare no competing financial interest. The findings and conclusions in this report are those of the author(s) and do not necessarily represent the official position of the National Institute for Occupational Safety and Health, Centers for Disease Control and Prevention.

CRediT authorship contribution statement

Ugochukwu Okoli: Validation, Formal analysis, Investigation, Writing – original draft, Writing – review & editing, Visualization. **Kabir Rishi:** Conceptualization, Methodology, Software, Investigation, Resources, Data curation, Writing – original draft, Writing – review & editing, Visualization, Supervision, Project administration. **Gregory Beaucage:** Conceptualization, Methodology, Software, Resources, Writing – review & editing, Visualization, Supervision, Project administration, Funding acquisition. **Hendrik K. Kammler:** Investigation. **Alex McGlasson:** Investigation. **Michael Chauby:** Investigation. **Vishak Narayanan:** Investigation. **James Grammens:** Investigation. **Vikram K. Kuppa:** Conceptualization, Methodology.

Declaration of competing interest

The authors declare the following financial interests/personal relationships which may be considered as potential competing interests: Gregory Beaucage reports financial support was provided by National Science Foundation. Gregory Beaucage reports financial support was provided by US Department of Energy Office of Science.

Data availability

Data will be made available on request.

Acknowledgements

This work was supported by the National Science Foundation through grants CMMI-1635865 and CMMI-1636036. Use of the Advanced Photon Source (APS), an Office of Science User Facility operated for the U.S. Department of Energy (DOE) Office of Science by Argonne National Laboratory, was supported by the U.S. DOE under contract no. DE-AC02-06CH11357. The USAXS data were collected at the APS on the beamline 9-ID-C operated by the X-ray Science Division. We gratefully acknowledge the vital assistance of Jan Ilavsky and Ivan Kuzmenko at beamline 9-ID-C. For use of the oscillatory rheometer and the FTIR spectrometer, we would like to thank Neil Ayres and Necati Kaval, respectively, in the Department of Chemistry at the University of Cincinnati.

Appendix A. Supplementary data

Supplementary data to this article can be found online at https://doi.org/10.1016/j.polymer.2022.125407.

References

[1] J.L. Leblanc, Rubber-filler interactions and rheological properties in filled compounds, Prog. Polym. Sci. 27 (2002) 627–687, https://doi.org/10.1016/S0079-6700(01)00040-5.
[2] P.G. Jeelani, P. Mulay, R. Venkat, C. Ramalingam, Multifaceted application of silica nanoparticles. A review,, Silicon 12 (2020) 1337–1354, https://doi.org/10.1007/s12633-019-00229-y.
[3] M.M. Fathy, F.M. Yassin, W.M. Elshemey, H.M. Fahmy, Insight on the dependence of the drug delivery applications of mesoporous silica nanoparticles on their physical properties, Silicon (2022), https://doi.org/10.1007/s12633-022-01962-7.
[4] P. Sae-oui, K. Suchiva, C. Sirisinha, W. Intiya, P. Yodjun, U. Thepsuwan, Effects of blend ratio and SBR type on properties of carbon black-filled and silica-filled SBR/BR tire tread compounds, Adv. Mater. Sci. Eng. 2017 (2017) 1–8, https://doi.org/10.1155/2017/2476101.
[5] G. Fontaras, N.G. Zacharof, B. Ciuffo, Fuel consumption and CO2 emissions from passenger cars in Europe - Laboratory versus real-world emissions, Prog. Energy Combust. Sci. 60 (2017) 97–131, https://doi.org/10.1016/j.pecs.2016.12.004.
[6] M.-J. Wang, Effect of polymer-filler and filler-filler interactions on dynamic properties of filled vulcanizates, Rubber Chem. Technol. 71 (1998) 520–589, https://doi.org/10.5254/1.3538492.
[7] X. Gao, W. Yang, C. Wang, X. Tian, Study on properties of carbon-coated silica prepared by polymer pyrolysis reinforced rubber composites, Polym. Test. 110 (2022) 107583, https://doi.org/10.1016/j.polymertesting.2022.107583.
[8] M. Hassanabadi, M. Najafi, S. Nikazar, S.S. Garakani, G.H. Motlagh, Impact of placement of aminopropyl triethoxy silane and tetraethoxy silicate on SSBR chains: analysis of rolling resistance, wet grip, and abrasion resistance, Adv. Polym. Technol. 2022 (2022), https://doi.org/10.1155/2022/1566042.
[9] W. Lei, X. Zhou, T.P. Russell, K. Hua, X. Yang, H. Qiao, W. Wang, F. Li, R. Wang, L. Zhang, High performance bio-based elastomers: energy efficient and sustainable

materials for tires, J. Mater. Chem. 4 (2016) 13058–13062, https://doi.org/10.1039/C6TA05001H.
[10] K. Rishi, V. Narayanan, G. Beaucage, A. McGlasson, V. Kuppa, J. Ilavsky, M. Rackaitis, A thermal model to describe kinetic dispersion in rubber nanocomposites: the effect of mixing time on dispersion, Polymer (Guildf) 175 (2019) 272–282, https://doi.org/10.1016/j.polymer.2019.03.044.
[11] A. McGlasson, K. Rishi, G. Beaucage, V. Narayanan, M. Chauby, A. Mulderig, V. K. Kuppa, J. Ilavsky, M. Rackaitis, The effects of staged mixing on the dispersion of reinforcing fillers in elastomer compounds, Polymer (Guildf) 181 (2019) 121765, https://doi.org/10.1016/j.polymer.2019.121765.
[12] D.C. Edwards, Polymer-filler interactions in rubber reinforcement, J. Mater. Sci. 25 (1990) 4175–4185, https://doi.org/10.1007/BF00581070.
[13] M. Castellano, L. Conzatti, G. Costa, L. Falqui, A. Turturro, B. Valenti, F. Negroni, Surface modification of silica: 1. Thermodynamic aspects and effect on elastomer reinforcement, Polymer (Guildf) 46 (2005) 695–703, https://doi.org/10.1016/j.polymer.2004.11.010.
[14] O. Aso, J.I. Eguiazábal, J. Nazábal, The influence of surface modification on the structure and properties of a nanosilica filled thermoplastic elastomer,, Compos. Sci. Technol. 67 (2007) 2854–2863, https://doi.org/10.1016/j.compscitech.2007.01.021.
[15] B.P. Kapgate, C. Das, D. Basu, A. Das, G. Heinrich, Rubber composites based on silane-treated stöber silica and nitrile rubber, J. Elastomers Plastics 47 (2015) 248–261, https://doi.org/10.1177/0095244313507807.
[16] H.A. Essawy, A.M. Khalil, M.E. Tawfik, S.H. El-Sabbagh, Compatibilization of NBR/SBR blends using amphiphilic montmorillonites: a dynamic mechanical thermal study,, J. Elastomers Plastics 46 (2014) 514–526, https://doi.org/10.1177/0095244313476507.
[17] H.A. Essawy, M.E. Tawfik, A.M. Khalil, S.H. El-Sabbagh, Systematic organophilization of montmorillonite: the impact thereof on the rheometric and mechanical characteristics of NBR and SBR based nanocomposites, Polym, Eng. Sci. 54 (2014) 942–948, https://doi.org/10.1002/pen.23632.
[18] A.M. Khalil, K.F. El-Nemr, M.L. Hassan, Acrylate-modified gamma-irradiated olive stones waste as a filler for acrylonitrile butadiene rubber/devulcanized rubber composites, J. Polym. Res. 26 (2019), https://doi.org/10.1007/s10965-019-1914-2.
[19] K. Rishi, L. Pallerla, G. Beaucage, A. Tang, Dispersion of surface-modified, aggregated, fumed silica in polymer nanocomposites, J. Appl. Phys. 127 (2020), https://doi.org/10.1063/1.5144252, 174702.
[20] A. McGlasson, K. Rishi, G. Beaucage, M. Chauby, V. Kuppa, J. Ilavsky, M. Rackaitis, Quantification of dispersion for weakly and strongly correlated nanofillers in polymer nanocomposites, Macromolecules 53 (2020) 2235–2248, https://doi.org/10.1021/acs.macromol.9b02429.
[21] Y. Li, X. Duan, C. Nie, Y. Jia, H. Zheng, The effect of polymer molecular weights on the electrical, rheological, and vapor sensing behavior of polycarbonate/multi-walled carbon nanotube nanocomposites, Polym. Compos. 43 (2022) 5095–5106, https://doi.org/10.1002/pc.26799.
[22] N. Ye, J. Zheng, X. Ye, J. Xue, D. Han, H. Xu, Z. Wang, L. Zhang, Performance enhancement of rubber composites using VOC-Free interfacial silica coupling agent, Compos. B Eng. 202 (2020) 108301, https://doi.org/10.1016/j.compositesb.2020.108301.
[23] M. Najam, M. Hussain, Z. Ali, I.M. Maafa, P. Akhter, K. Majeed, A. Ahmed, N. Shehzad, Influence of silica materials on synthesis of elastomer nanocomposites: a review, J. Elastomers Plastics 52 (2020) 747–771, https://doi.org/10.1177/0095244319888768.
[24] X. Wang, L. Wu, H. Yu, T. Xiao, H. Li, J. Yang, Modified silica-based isoprene rubber composite by a multi-functional silane: preparation and its mechanical and dynamic mechanical properties, Polym. Test. 91 (2020) 106840, https://doi.org/10.1016/j.polymertesting.2020.106840.
[25] S.K. Kumar, N. Jouault, B. Benicewicz, T. Neely, Nanocomposites with polymer grafted nanoparticles, Macromolecules 46 (2013) 3199–3214, https://doi.org/10.1021/ma4001385.
[26] G.P. Baeza, A.C. Genix, C. Degrandcourt, L. Petitjean, J. Gummel, M. Couty, J. Oberdisse, Multiscale filler structure in simplified industrial nanocomposite silica/SBR systems studied by SAXS and TEM, Macromolecules 46 (2013) 317–329, https://doi.org/10.1021/ma302248p.
[27] T. Hashimoto, N. Amino, S. Nishitsuji, M. Takenaka, Hierarchically self-organized filler particles in polymers: cascade evolution of dissipative structures to ordered structures, Polym. J. 51 (2019) 109–130, https://doi.org/10.1038/s41428-018-0147-2.
[28] K. Rishi, G. Beaucage, V. Kuppa, A. Mulderig, V. Narayanan, A. McGlasson, M. Rackaitis, J. Ilavsky, Impact of an emergent hierarchical filler network on nanocomposite dynamics, Macromolecules 51 (2018) 7893–7904, https://doi.org/10.1021/acs.macromol.8b01510.
[29] L. Song, Z. Wang, X. Tang, L. Chen, P. Chen, Q. Yuan, L. Li, Visualizing the toughening mechanism of nanofiller with 3D X-ray nano-CT: stress-induced phase separation of silica nanofiller and silicone polymer double networks, Macromolecules 50 (2017) 7249–7257, https://doi.org/10.1021/acs.macromol.7b00539.
[30] G. Filippone, M. Salzano De Luna, A unifying approach for the linear viscoelasticity of polymer nanocomposites,, Macromolecules 45 (2012) 8853–8860, https://doi.org/10.1021/ma301594g.
[31] G. Filippone, G. Romeo, D. Acierno, Viscoelasticity and structure of polystyrene/fumed silica nanocomposites: filler network and hydrodynamic contributions, Langmuir 26 (2010) 2714–2720, https://doi.org/10.1021/la902755r.
[32] J.J. Richards, J.B. Hipp, J.K. Riley, N.J. Wagner, P.D. Butler, Clustering and percolation in suspensions of carbon black, Langmuir 33 (2017) 12260–12266, https://doi.org/10.1021/acs.langmuir.7b02538.
[33] C. Zhang, Z. Tang, B. Guo, L. Zhang, Concurrently improved dispersion and interfacial interaction in rubber/nanosilica composites via efficient hydrosilane functionalization, Compos. Sci. Technol. 169 (2019) 217–223, https://doi.org/10.1016/j.compscitech.2018.11.016.
[34] C.C. Liu, G.E. Maciel, The fumed silica surface: a study by NMR,, J. Am. Chem. Soc. 118 (1996) 5103–5119, https://doi.org/10.1021/ja954120w.
[35] A. Krysztafkiewicz, B. Rager, T. Jesionowski, The effect of surface modification on physicochemical properties of precipitated silica,, J. Mater. Sci. 32 (1997) 1333–1339, https://doi.org/10.1023/A:1018564808810.
[36] I. Mora-Barrantes, A. Rodríguez, L. Ibarra, L. González, J.L. Valentín, Overcoming the disadvantages of fumed silica as filler in elastomer composites, J. Mater. Chem. 21 (2011) 7381–7392, https://doi.org/10.1039/c1jm10410a.
[37] K. Luo, W. Zheng, X. Zhao, X. Wang, S. Wu, Effects of antioxidant functionalized silica on reinforcement and anti-aging for solution-polymerized styrene butadiene rubber: experimental and molecular simulation study, Mater. Des. 154 (2018) 312–325, https://doi.org/10.1016/j.matdes.2018.05.048.
[38] M. Castellano, L. Conzatti, A. Turturro, G. Costa, G. Busca, Influence of the silane modifiers on the surface thermodynamic characteristics and dispersion of the silica into elastomer compounds, J. Phys. Chem. B 111 (2007) 4495–4502, https://doi.org/10.1021/jp0702144.
[39] J. Liu, S. Wu, M. Zou, X. Zheng, Z. Cai, Surface modification of silica and its compounding with polydimethylsiloxane matrix: interaction of modified silica filler with PDMS, Iran. Polym. J. (Engl. Ed.) 21 (2012) 583–589, https://doi.org/10.1007/s13726-012-0062-x.
[40] Y. Li, B. Han, S. Wen, Y. Lu, H. Yang, L. Zhang, L. Liu, Effect of the temperature on surface modification of silica and properties of modified silica filled rubber composites, Compos. Part A Appl. Sci. Manuf 62 (2014) 52–59, https://doi.org/10.1016/j.compositesa.2014.03.007.
[41] H. Yao, G. Weng, Y. Liu, K. Fu, A. Chang, Z.-R. Chen, Effect of silane coupling agent on the fatigue crack propagation of silica-filled natural rubber, J. Appl. Polym. Sci. 132 (2015), https://doi.org/10.1002/app.41980, 41980.
[42] R. Mueller, H.K. Kammler, S.E. Pratsinis, A. Vital, G. Beaucage, P. Burtscher, Non-agglomerated dry silica nanoparticles, Powder Technol. 140 (2004) 40–48, https://doi.org/10.1016/j.powtec.2004.01.004.
[43] H.K. Kammler, R. Mueller, O. Senn, S.E. Pratsinis, Synthesis of silica-carbon particles in a turbulent H2-air flame aerosol reactor, AIChE J. 47 (2001) 1533–1543, https://doi.org/10.1002/aic.690470707.
[44] G. Beaucage, D.W.W. Schaefer, Structural studies of complex systems using small-angle scattering: a unified Guinier/power-law approach, J. Non-Cryst. Solids 172–174 (1994) 797–805, https://doi.org/10.1016/0022-3093(94)90581–90589.
[45] G. Beaucage, Approximations leading to a unified exponential/power-law approach to small-angle scattering, J. Appl. Crystallogr. 28 (1995) 717–728, https://doi.org/10.1107/S0021889895005292.
[46] G. Beaucage, T.A. Ulibarri, E.P. Black, D.W. Schaefer, Multiple size scale structures in silica-siloxane composites studied by small-angle scattering, in: Hybrid Org. Compos, 1995, pp. 97–111, https://doi.org/10.1021/bk-1995-0585.ch009.
[47] C.M. Sorensen, G.M. Wang, Size distribution effect on the power law regime of the structure factor of fractal aggregates, Phys. Rev. E 60 (1999) 7143–7148, https://doi.org/10.1103/PhysRevE.60.7143.
[48] K. Vogtt, G. Beaucage, M. Weaver, H. Jiang, Thermodynamic stability of worm-like micelle solutions, Soft Matter 13 (2017) 6068–6078, https://doi.org/10.1039/c7sm01132f.
[49] Y. Jin, G. Beaucage, K. Vogtt, H. Jiang, V. Kuppa, J. Kim, J. Ilavsky, M. Rackaitis, A. Mulderig, K. Rishi, V. Narayanan, A pseudo-thermodynamic description of dispersion for nanocomposites, Polymer (Guildf) 129 (2017) 32–43, https://doi.org/10.1016/j.polymer.2017.09.040.
[50] J. Van Rijssel, V.F.D. Peters, J.D. Meeldijk, R.J. Kortschot, R.J.A. Van Dijk-Moes, A. V. Petukhov, B.H. Erné, A.P. Philipse, Size-dependent second virial coefficients of quantum dots from quantitative cryogenic electron microscopy, J. Phys. Chem. B 118 (2014) 11000–11005, https://doi.org/10.1021/jp5056182.
[51] T. Glaskova, M. Zarrelli, A. Aniskevich, M. Giordano, L. Trinkler, B. Berzina, Quantitative optical analysis of filler dispersion degree in MWCNT-epoxy nanocomposite, Compos. Sci. Technol. 72 (2012) 477–481, https://doi.org/10.1016/j.compscitech.2011.11.029.
[52] A. Dorigato, M. D'Amato, A. Pegoretti, Thermo-mechanical properties of high density polyethylene - fumed silica nanocomposites: effect of filler surface area and treatment, J. Polym. Res. 19 (2012) 9889, https://doi.org/10.1007/s10965-012-9889-2.
[53] S. Pfeifer, P.R. Bandaru, A methodology for quantitatively characterizing the dispersion of nanostructures in polymers and composites,, Mater. Res. Lett. 2 (2014) 166–175, https://doi.org/10.1080/21663831.2014.886629.
[54] J. Liu, Y. Gao, D. Cao, L. Zhang, Z. Guo, Nanoparticle dispersion and aggregation in polymer nanocomposites: insights from molecular dynamics simulation, Langmuir 27 (2011) 7926–7933, https://doi.org/10.1021/la201073m.
[55] R. Mueller, H.K. Kammler, K. Wegner, S.E. Pratsinis, OH surface density of SiO 2 and TiO 2 by thermogravimetric analysis, Langmuir 19 (2003) 160–165, https://doi.org/10.1021/la025785w.
[56] M. Bousmina, A. Ait-Kadi, J.B. Faisant, Determination of shear rate and viscosity from batch mixer data, J. Rheol. (N. Y. N. Y) 43 (1999) 415–433, https://doi.org/10.1122/1.551044.
[57] S. Sadhu, A.K. Bhowmick, Unique rheological behavior of rubber based nanocomposites, J. Polym. Sci., Part B: Polym. Phys. 43 (2005) 1854–1864, https://doi.org/10.1002/polb.20469.

[58] J. Ilavsky, F. Zhang, R.N. Andrews, I. Kuzmenko, P.R. Jemian, L.E. Levine, A. J. Allen, Development of combined microstructure and structure characterization facility for in situ and operando studies at the advanced photon source, J. Appl. Crystallogr. 51 (2018) 867–882, https://doi.org/10.1107/S160057671800643X.
[59] J. Ilavsky, P.R. Jemian, Irena : tool suite for modeling and analysis of small-angle scattering, J. Appl. Crystallogr. 42 (2009) 347–353, https://doi.org/10.1107/S0021889809002222.
[60] A. Mulderig, G. Beaucage, K. Vogtt, H. Jiang, V. Kuppa, Quantification of branching in fumed silica, J. Aerosol Sci. 109 (2017) 28–37, https://doi.org/10.1016/j.jaerosci.2017.04.001.
[61] G. Beaucage, H.K. Kammler, S.E. Pratsinis, Particle size distributions from small-angle scattering using global scattering functions, J. Appl. Crystallogr. 37 (2004) 523–535, https://doi.org/10.1107/S0021889804008969.
[62] H.K. Kammler, G. Beaucage, D.J. Kohls, N. Agashe, J. Ilavsky, Monitoring simultaneously the growth of nanoparticles and aggregates by in situ ultra-small-angle x-ray scattering, J. Appl. Phys. 97 (2005), https://doi.org/10.1063/1.1855391.
[63] K. Vogtt, G. Beaucage, M. Weaver, H. Jiang, Scattering function for branched wormlike chains, Langmuir 31 (2015) 8228–8234, https://doi.org/10.1021/acs.langmuir.5b01630.
[64] Evonik, Aerosil 200. https://products-re.evonik.com/www2/uploads/productfinder/AEROSIL-200-EN.pdf. (Accessed 20 May 2022).
[65] M. Endo, K. Takeuchi, T. Hiraoka, T. Furuta, T. Kasai, X. Sun, C.H. Kiang, M. S. Dresselhaus, Stacking nature of graphene layers in carbon nanotubes and nanofibres, J. Phys. Chem. Solid. 58 (1997) 1707–1712, https://doi.org/10.1016/S0022-3697(97)00055-3.
[66] P.D. Lickiss, The synthesis and structure of organosilanols, Ed., in: A.G. Sykes (Ed.), Adv. Inorg. Chem., Academic Press, 1995, pp. 147–262, https://doi.org/10.1016/S0898-8838(08)60053-7. vol. 42
[67] J. Demaison, M. Herman, J. Lievin, The equilibrium OH bond length,, Int. Rev. Phys. Chem. 26 (2007) 391–420, https://doi.org/10.1080/01442350701371919.
[68] Y. Shui, L. Huang, C. Wei, G. Sun, J. Chen, A. Lu, L. Sun, D. Liu, How the silica determines properties of filled silicone rubber by the formation of filler networking and bound rubber, Compos. Sci. Technol. 215 (2021), https://doi.org/10.1016/j.compscitech.2021.109024.
[69] H.M. Smallwood, Limiting law of the reinforcement of rubber, J. Appl. Phys. 15 (1944) 758–766, https://doi.org/10.1063/1.1707385.
[70] E. Guth, Theory of filler reinforcement, J. Appl. Phys. 16 (1945) 20–25, https://doi.org/10.1063/1.1707495.
[71] A.J. Hughes, The Einstein relation between relative viscosity and volume concentration of suspensions of spheres,, Nature 173 (1954) 1089–1090, https://doi.org/10.1038/1731089a0.
[72] A.I. Medalia, Morphology of aggregates: VI. Effective volume of aggregates of carbon black from electron microscopy; Application to vehicle absorption and to die swell of filled rubber, J. Colloid Interface Sci. 32 (1970) 115–131, https://doi.org/10.1016/0021-9797(70)90108-6.
[73] A.I. Medalia, Effective degree of immobilization of rubber occluded within carbon black aggregates, Rubber Chem. Technol. 45 (1972) 1171–1194, https://doi.org/10.5254/1.3544731.
[74] C.F.S. Gabriel, A, de A.P. Gabino, A.M.F. de Sousa, C.R.G. Furtado, R.C.R. Nunes, Tire tread rubber compounds with ternary system filler based on carbon black, silica, and metakaolin: contribution of silica/metakaolin content on the final properties, J. Elastomers Plastics 51 (2019) 712–726, https://doi.org/10.1177/0095244318819196.
[75] S. Sattayanurak, J.W.M. Noordermeer, K. Sahakaro, W. Kaewsakul, W.K. Dierkes, A. Blume, Silica-Reinforced natural rubber: synergistic effects by addition of small amounts of secondary fillers to silica-reinforced natural rubber tire tread compounds, Adv. Mater. Sci. Eng. 2019 (2019) 1–8, https://doi.org/10.1155/2019/5891051.

Dispersion of modified fumed silica in elastomeric nanocomposites.

Ugochukwu Okoli[1#], Kabir Rishi[2#], Gregory Beaucage[1*], Hendrik K. Kammler[3], Alex McGlasson[4], Michael Chauby[5], Vishak Narayanan[6], James Grammens[1], Vikram K. Kuppa[7]

[1] Chemical & Materials Engineering, University of Cincinnati, Cincinnati OH 45242-0012, United States

[2] Centers for Disease Control and Prevention, National Institute for Occupational Safety and Health, Cincinnati, OH 45213, United States

[3] Novartis Pharma AG, Postfach, CH-4002 Basel, Switzerland

[4] Polymer Science & Engineering, University of Massachusetts, Amherst MA 01003, United States

[5] Chemical Engineering, Drexel University, Philadelphia PA 19104, United States

[6] Reliance Industries Ltd., Elastomer Business Group, Navi Mumbai, Maharashtra 400701, India

[7] Nonstructural Materials Division, University of Dayton Research Institute, Dayton OH 45469

[#]Equal contribution by U.O. & K.R.

Supplementary Information

Appendix A

Table T1. Surface carbon content (wt.%) from elemental analysis and thermogravimetric analysis (TGA); specific surface area (m2/g) through BET measurements, and experimental details during carbon-coated silica synthesis.

Surface carbon (wt.%) – Elemental analysis	Surface carbon (wt.%) – TGA[a]	Specific surface area (m2/g) – BET[a]	Flow rate (l/min)[b]			T_{HMDSO} (°C)[b]	Flame height (cm)[b]
			HMDSO / N_2	H_2 (both tubes)	Air		
0.37	0.25	122	10	1	-	-	-
0.74	0.49	122			120	33	45
0.86	0.54	108			103	35	45
2.03	1.55	75			103	54	60-70

[a] detail of TGA and BET measurements given in (Kammler et al., 2001; Mueller et al., 2003, 2004).

[b] detail of the flow rate of the precursor gas, hydrogen and sheath air, temperature of the HMDSO precursor, and flame height during the synthesis of carbon-coated silica nanoparticles in flame

Figure S1 shows the FTIR absorbance spectra of the fumed silica powders. From Figure S1 inset, it is observed that all grades show a broad peak between 3000–3600cm^{-1}. Additionally, each grade of fumed silica shows sharp peaks lying between 950–1300cm^{-1}, 750–900cm^{-1} and 400–530cm^{-1}, which are associated with the antisymmetric and symmetric stretching vibration of Si–O–Si and the deformation vibration of O–Si–O, respectively (Brinker & Scherer, 1990; Duran et al., 1986; Gottardi et al., 1984; McDonald, 1958). The ratio of the OH peak area between 3000–3600cm^{-1} and the Si–O–Si peak area between 950–1300cm^{-1} along with the primary particle size, d_p, from USAXS analysis is used to determine the surface silanol content in Table 1 following Rishi et al. (Rishi et al., 2020).

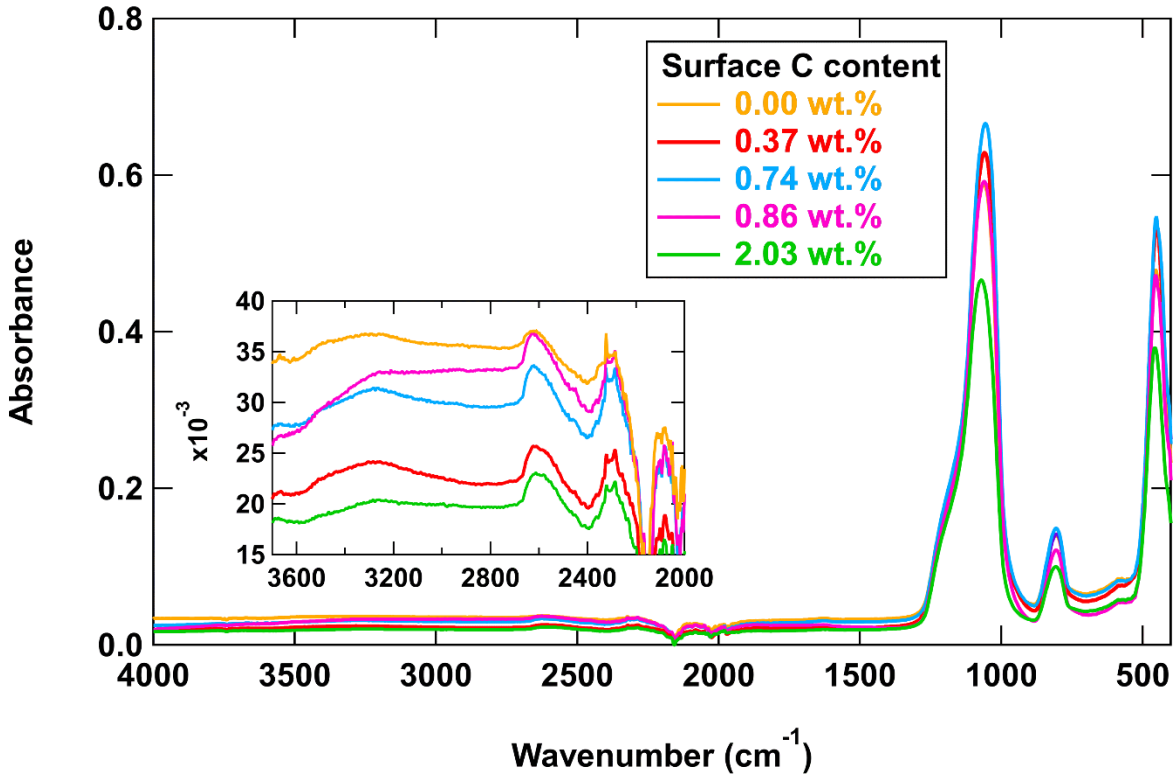

Figure S1. FTIR spectra of the modified fumed silica powders showing the characteristic Si-O peaks; the inset shows the broad hydroxyl peaks associated with surface silanols.

Appendix B

Table T2. Unified Fit parameters for primary particle and aggregate, structural levels 1 and 2 respectively from fits to the $I_0(q)/\phi_0$ at dilute silica concentration $\phi_0 \approx 0.0043$. The fits are shown in Figures 6, S1-S4.

Surface carbon content (wt.%)	**Primary particle level**				**Aggregate level**			
	G_1 ($\times 10^5$ cm^{-1})	$R_{g,1}$ (Å)	b_1 ($\times 10^{-4}$ $cm^{-1}Å^{-P_1}$)	P_1	G_2 ($\times 10^7$ cm^{-1})	$R_{g,2}$ (Å)	b_2 ($cm^{-1}Å^{-P_2}$)	P_2
0	0.4 (±0.03)	120 (±3)	25.5 (±0.3)	4	2.3 (±0.3)	2200 (±150)	0.5 (±0.07)	2.5 (±0.03)
0.37	1.1 (±0.02)	180 (±3)	15 (±1)	4	3 (±0.3)	2350 (±100)	1.5 (±0.1)	2.3 (±0.01)
0.74	0.8 (±0.1)	190 (±8)	11 (±0.5)	4	2.2 (±0.5)	2300 (±90)	2.7 (±0.2)	2.2 (±0.02)
0.86	1.7 (±0.2)	240 (±10)	10.5 (±0.3)	4	3.3 (±0.7)	2600 (±200)	6 (±1)	2.1 (±0.03)
2.03	6 (±2)	350 (±30)	6.9 (±0.01)	4	7 (±2)	3600 (±500)	22 (±9)	1.9 (±0.06)

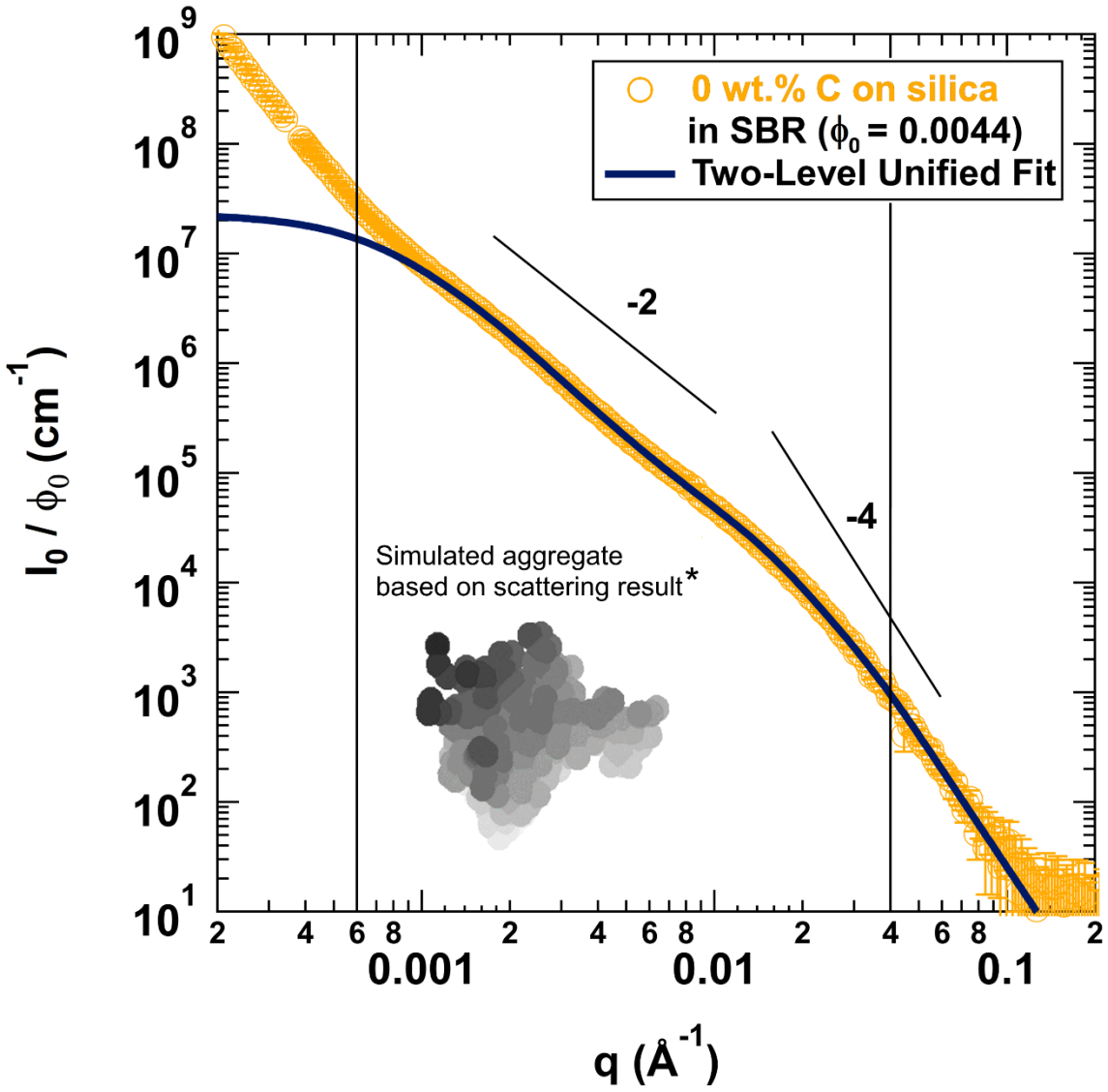

Figure S2. Log-Log plot of the reduced scattered intensity, $I_0(q)/\phi_0$ vs q (scattering vector) for commercial fumed silica coated with 0 wt.% of carbon in the SBR polymer matrix under dilute ($\phi_0 \approx 0.0044$) concentrations. A simulated aggregate structure (Mulderig et al., 2017) that agrees with the aggregate topological parameters based on the Unified Fit (Beaucage, 1995; Beaucage & Schaefer, 1994) results, eq. 1.

*The image of the simulated aggregate Reprinted from K. Rishi, L. Pallerla, G. Beaucage, A. Tang, Dispersion of surface-modified, aggregated, fumed silica in polymer nanocomposites, J. Appl. Phys. 127 (2020) 174702 with the permission of AIP Publishing. (Rishi et al., 2020).

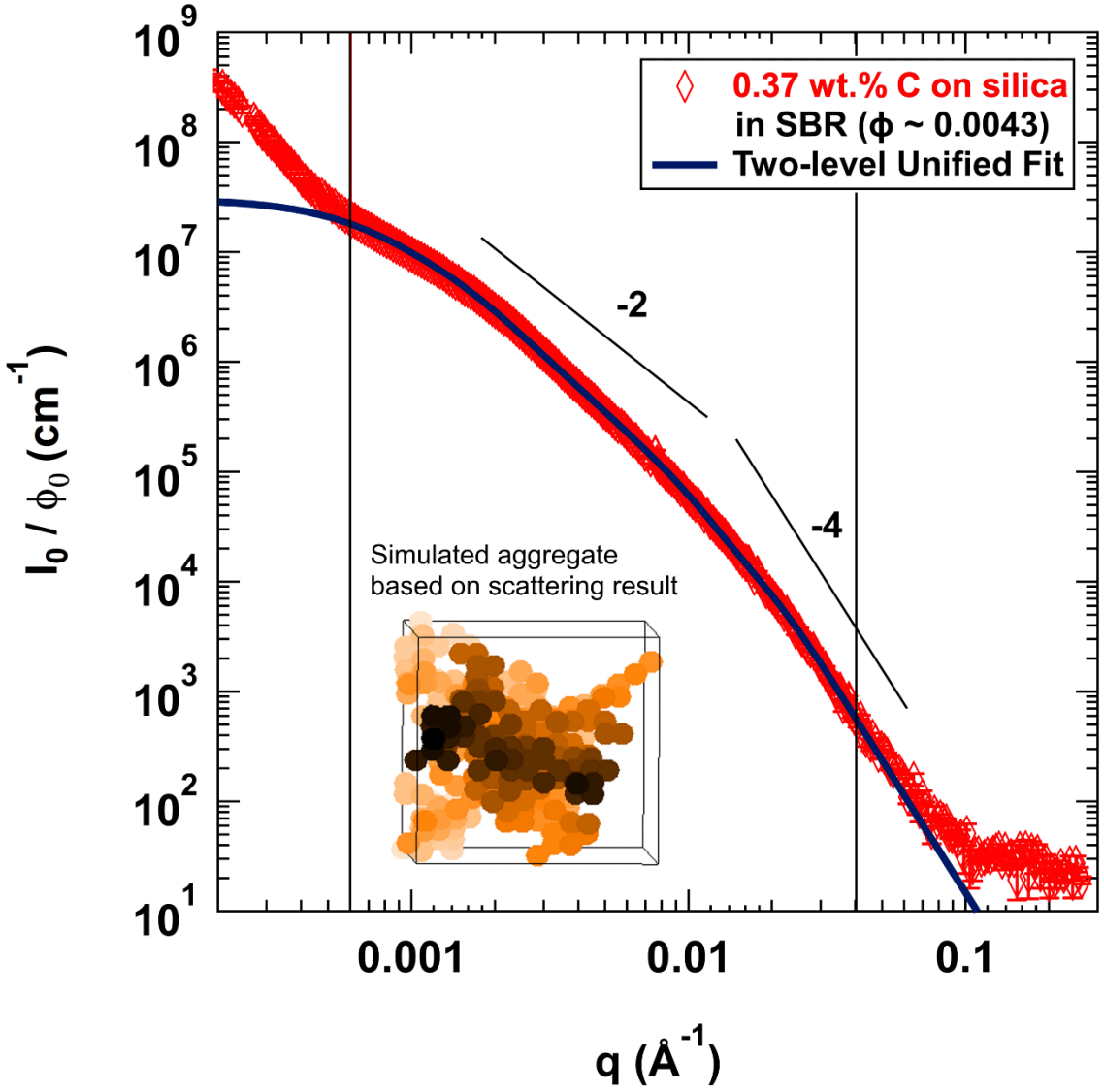

Figure S3. Log-Log plot of the reduced scattered intensity, $I_0(q)/\phi_0$ vs q (scattering vector) for the flame-synthesized silica nanofiller coated with 0.37 wt.% of carbon in the SBR polymer matrix under dilute ($\phi_0 \approx 0.0043$) concentrations. A simulated aggregate structure (Mulderig et al., 2017) that agrees with the aggregate topological parameters based on the Unified Fit (Beaucage, 1995; Beaucage & Schaefer, 1994) results, eq. 1.

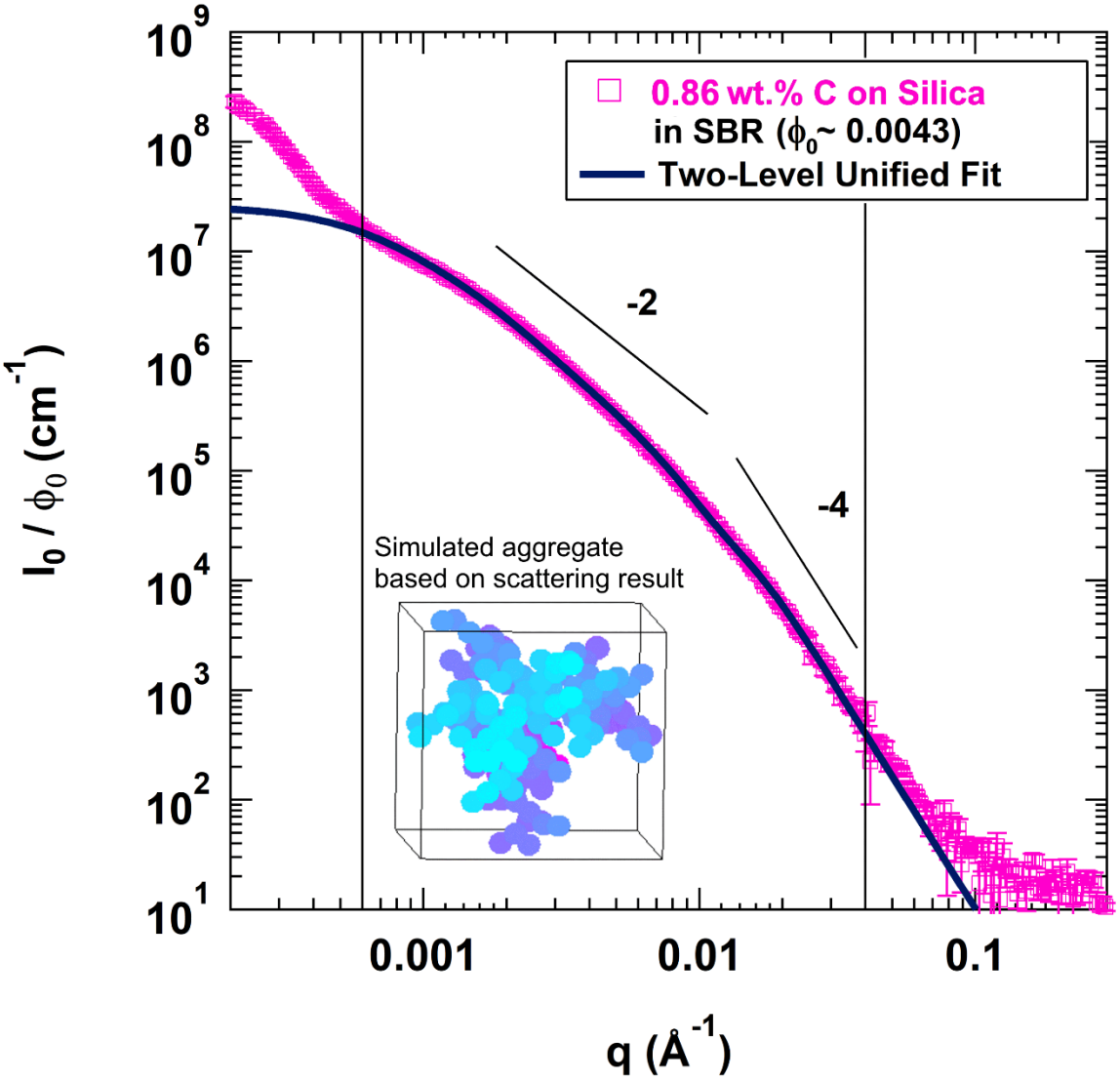

Figure S4. Log-Log plot of the reduced scattered intensity, $I_0(q)/\phi_0$ vs q (scattering vector) for the flame-synthesized silica nanofiller coated with 0.86 wt.% of carbon in the SBR polymer matrix under dilute ($\phi_0 \approx 0.0043$) concentrations. A simulated aggregate structure (Mulderig et al., 2017) that agrees with the aggregate topological parameters based on the Unified Fit (Beaucage, 1995; Beaucage & Schaefer, 1994) results, eq. 1.

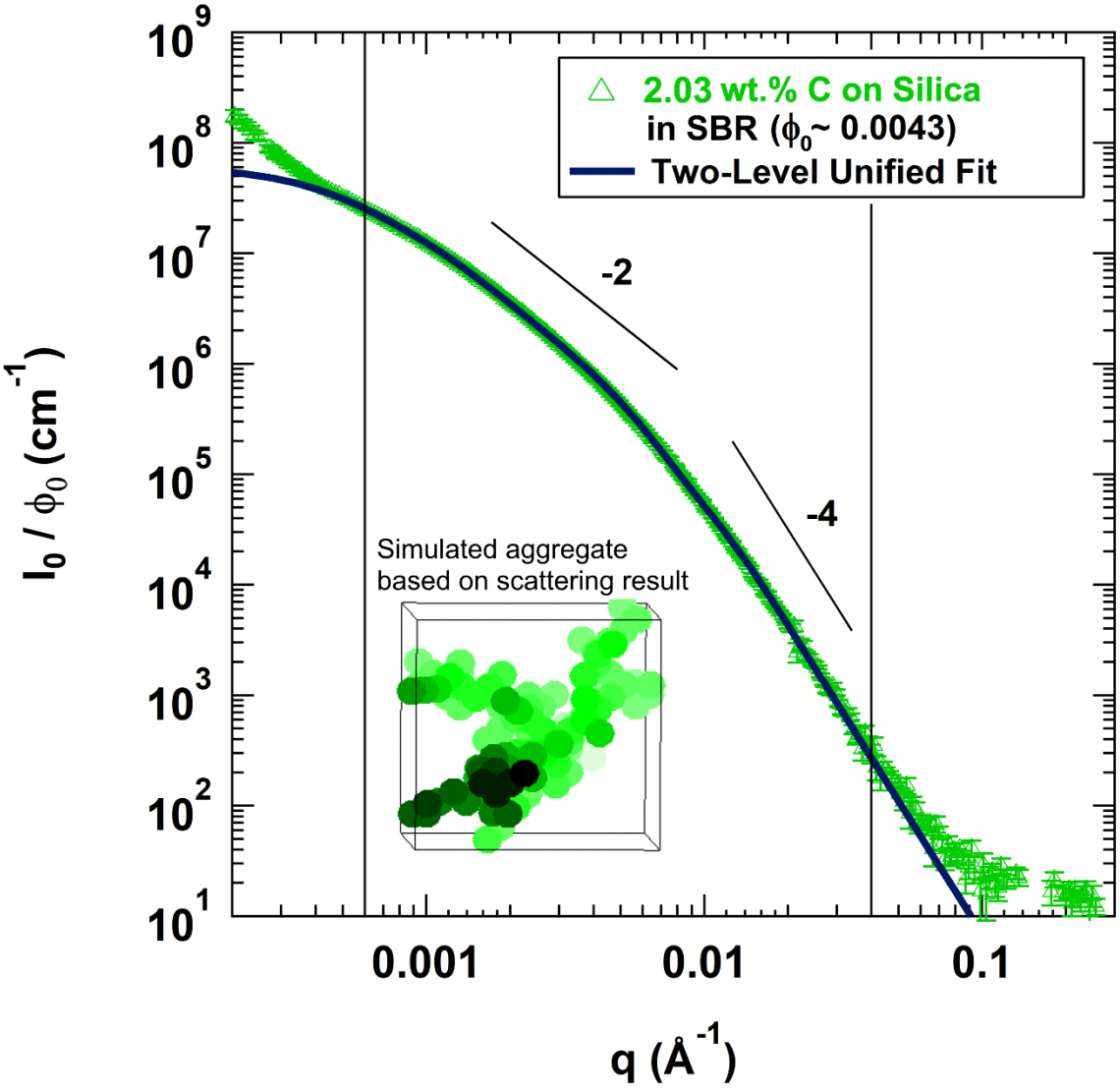

Figure S5. Log-Log plot of the reduced scattered intensity, $I_0(q)/\phi_0$ vs q (scattering vector) for the flame-synthesized silica nanofiller coated with 2.03 wt.% of carbon in the SBR polymer matrix under dilute ($\phi_0 \approx 0.0043$) concentrations. A simulated aggregate structure (Mulderig et al., 2017) that agrees with the aggregate topological parameters based on the Unified Fit (Beaucage, 1995; Beaucage & Schaefer, 1994) results, eq. 1.

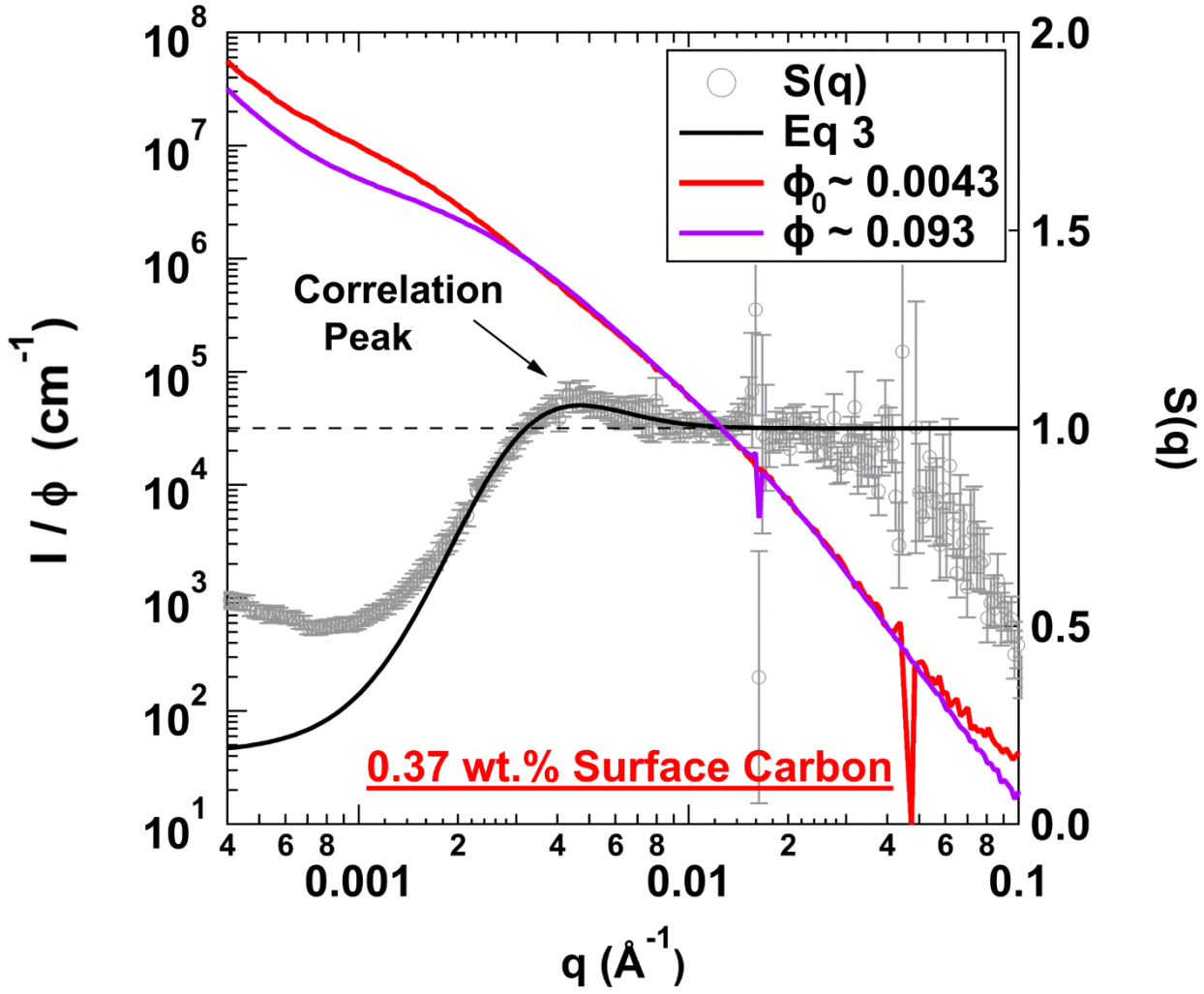

Figure S6. Log-log plot of the reduced scattered intensities, $I_0(q)/\phi_0$ and $I(q)/\phi$ (read from the left ordinate) and the inter-particle structure factor, $S(q)$ (read from the right ordinate) as a function of the scattering vector q for modified silica nanofillers with 0.37 wt.% surface carbon content in SBR. Note that ϕ_0 and ϕ represent the dilute and semi-dilute filler concentrations, respectively, as listed in the plot. A broad peak at intermediate q in the $S(q)$ plots, indicates the emergence of correlated aggregates.

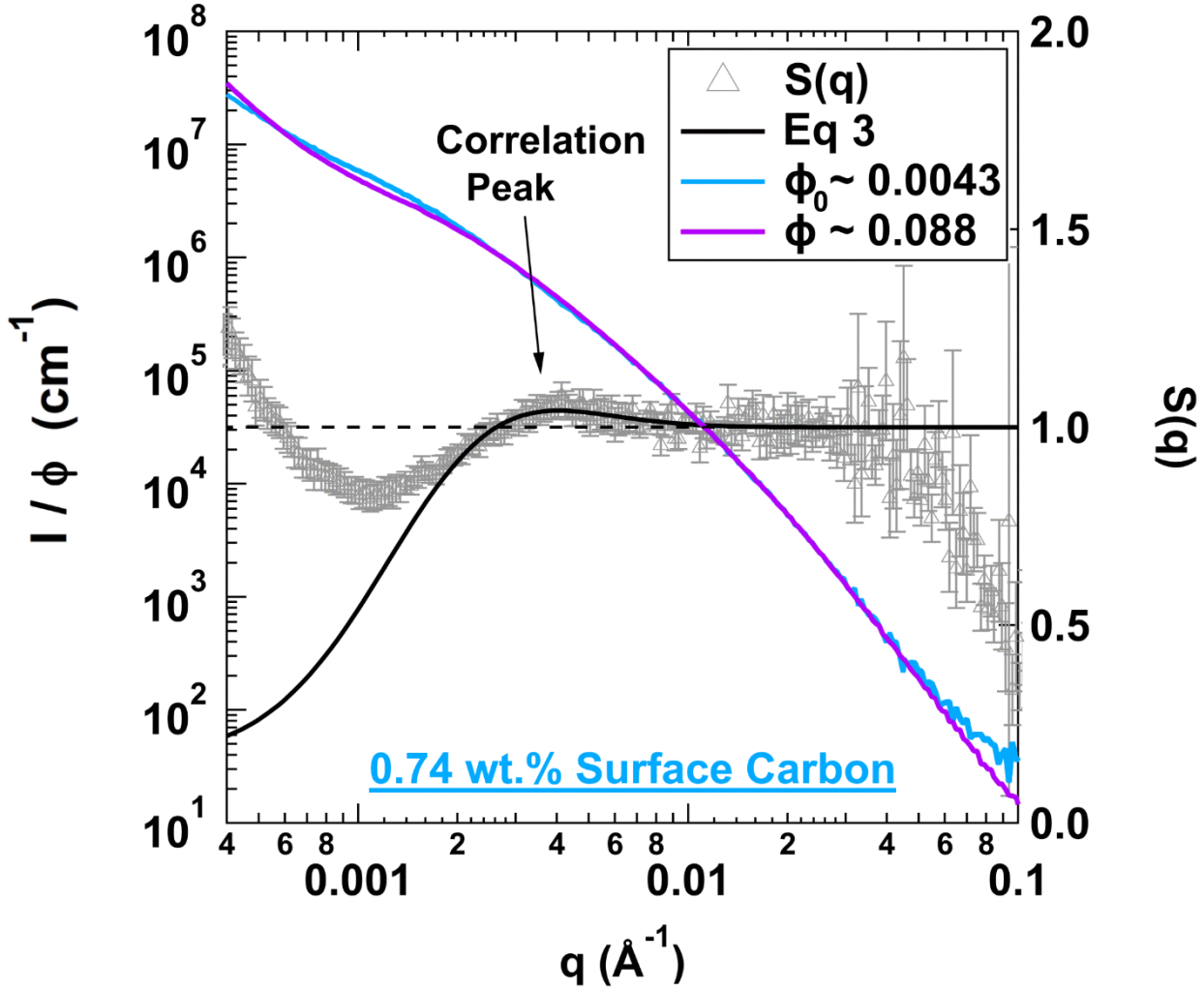

Figure S7. Log-log plot of the reduced scattered intensities, $I_0(q)/\phi_0$ and $I(q)/\phi$ (read from the left ordinate) and the inter-particle structure factor, $S(q)$ (read from the right ordinate) as a function of the scattering vector q for modified silica nanofillers with 0.74 wt.% surface carbon content in SBR. Note that ϕ_0 and ϕ represent the dilute and semi-dilute filler concentrations, respectively, as listed in the plot. A broad peak at intermediate q in the $S(q)$ plots, indicates the emergence of correlated aggregates.

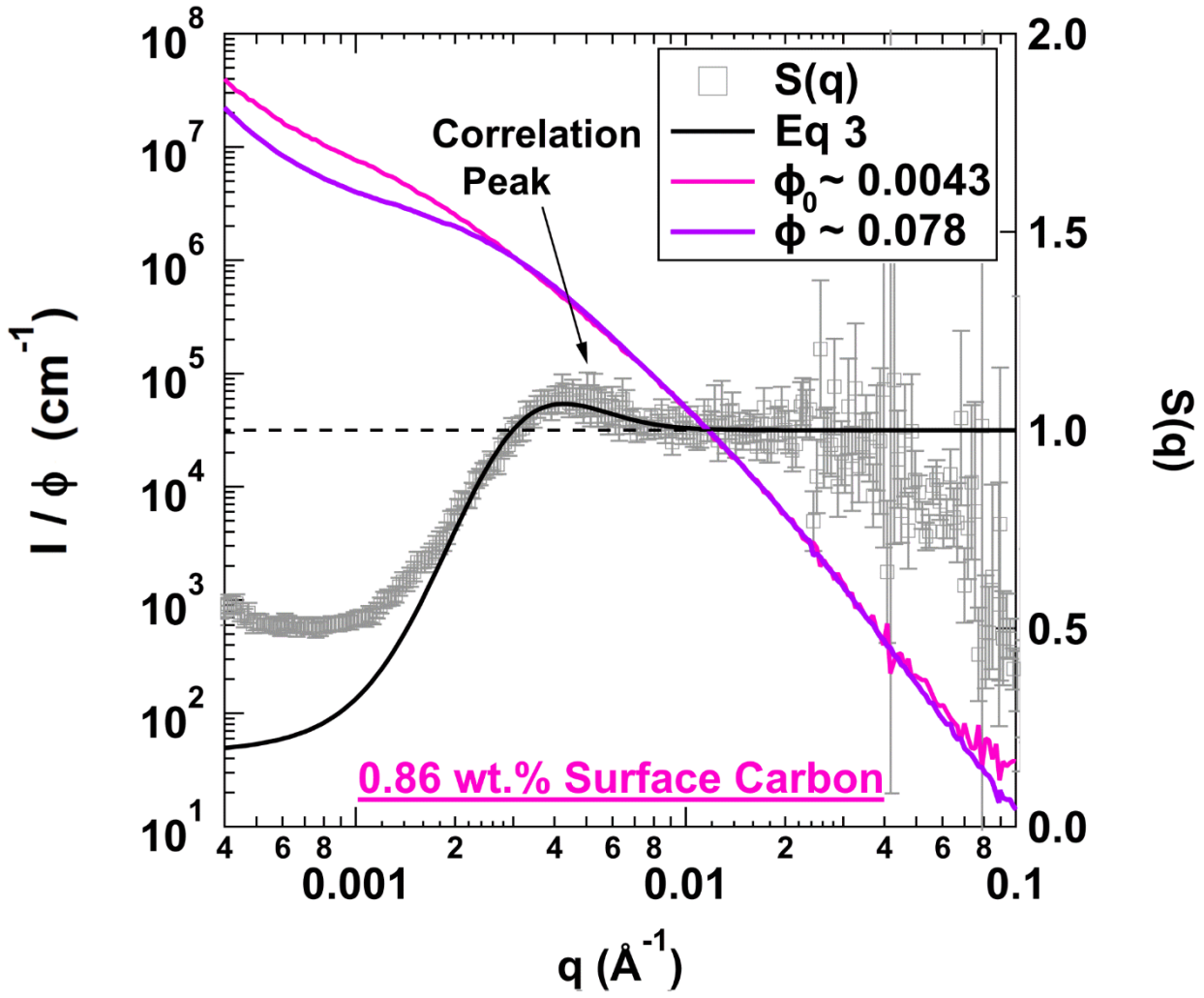

Figure S8. Log-log plot of the reduced scattered intensities, $I_0(q)/\phi_0$ and $I(q)/\phi$ (read from the left ordinate) and the inter-particle structure factor, $S(q)$ (read from the right ordinate) as a function of the scattering vector q for modified silica nanofillers with 0.86 wt.% surface carbon content in SBR. Note that ϕ_0 and ϕ represent the dilute and semi-dilute filler concentrations, respectively, as listed in the plot. A broad peak at intermediate q in the $S(q)$ plots, indicates the emergence of correlated aggregates.

Appendix C

Figures S9-S14 show a plot of the storage (G') and loss (G'') moduli master curves after time-temperature superposition for neat, 0 wt.%, 0.37 wt.%, 0.74 wt.%, 0.86 wt.% and 2.03 wt.% carbon coated silica in SBR at ~0.09 volume fraction filler (semi-dilute) and at a reference temperature of 25°C. The shift factors, a_T, were determined experimentally by overlapping the curves using a least squares routine. The logarithm of a_T was then fit using the WLF equation as shown in inset figures in S9-S14 to obtain the WLF-parameters C_1 and C_2. A good overlap of the moduli curves over the experimental range indicates that the WLF constants determined from the experimental a_T values are reasonable.

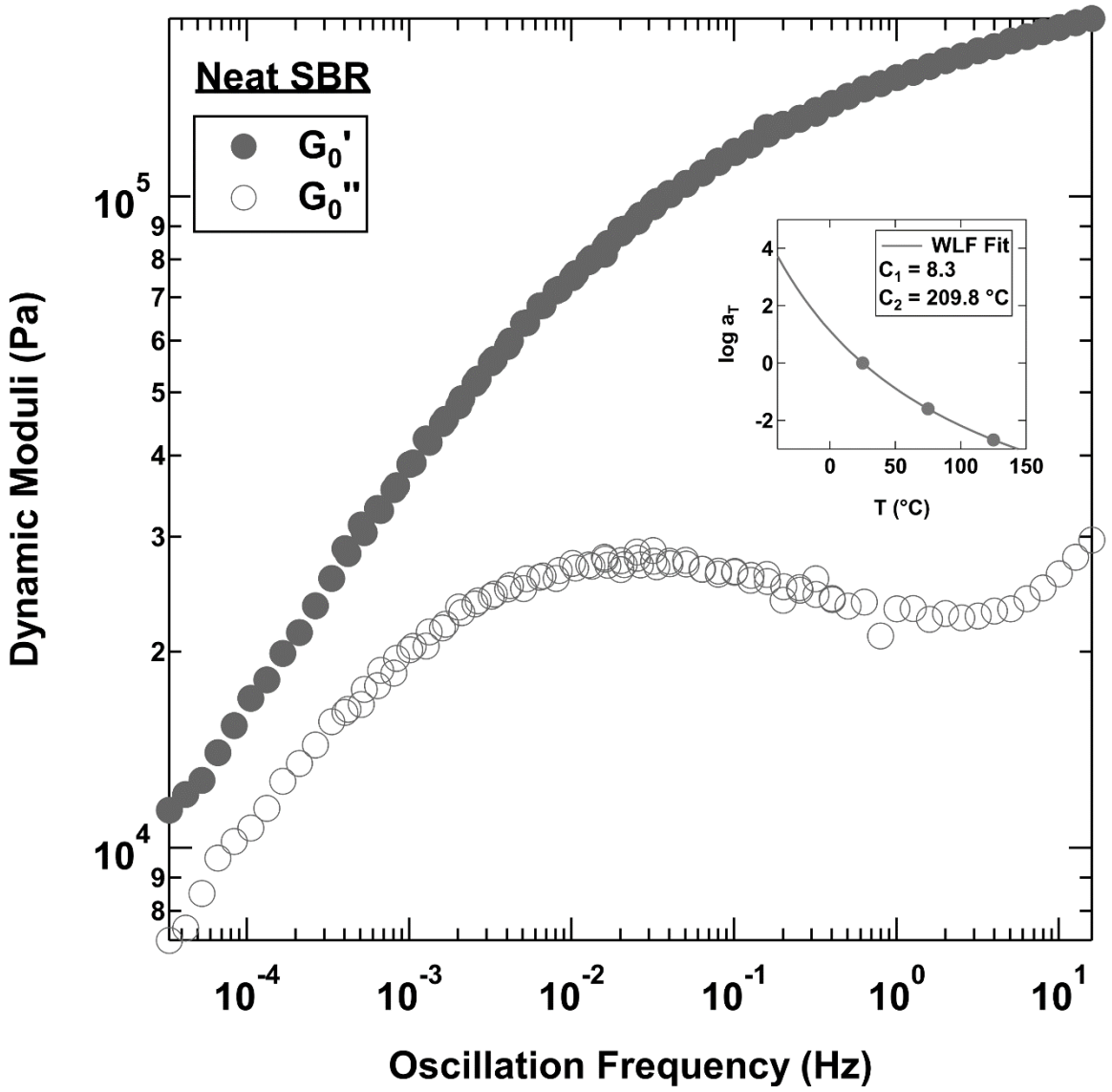

Figure S9. Plot of dynamic moduli, $G_0{}'$ (storage) and $G_0{}''$ (loss) versus oscillation frequency, ω for the neat styrene butadiene rubber (ϕ = 0 volume fraction of filler) at a reference temperature of 25°C. Note that the master curves were constructed from isothermal frequency sweeps at 25°C, 75°C and 125°C. The experimental shift factors were fit using the WLF model to ascertain the constants, C_1 and C_2 as shown in the inset figure.

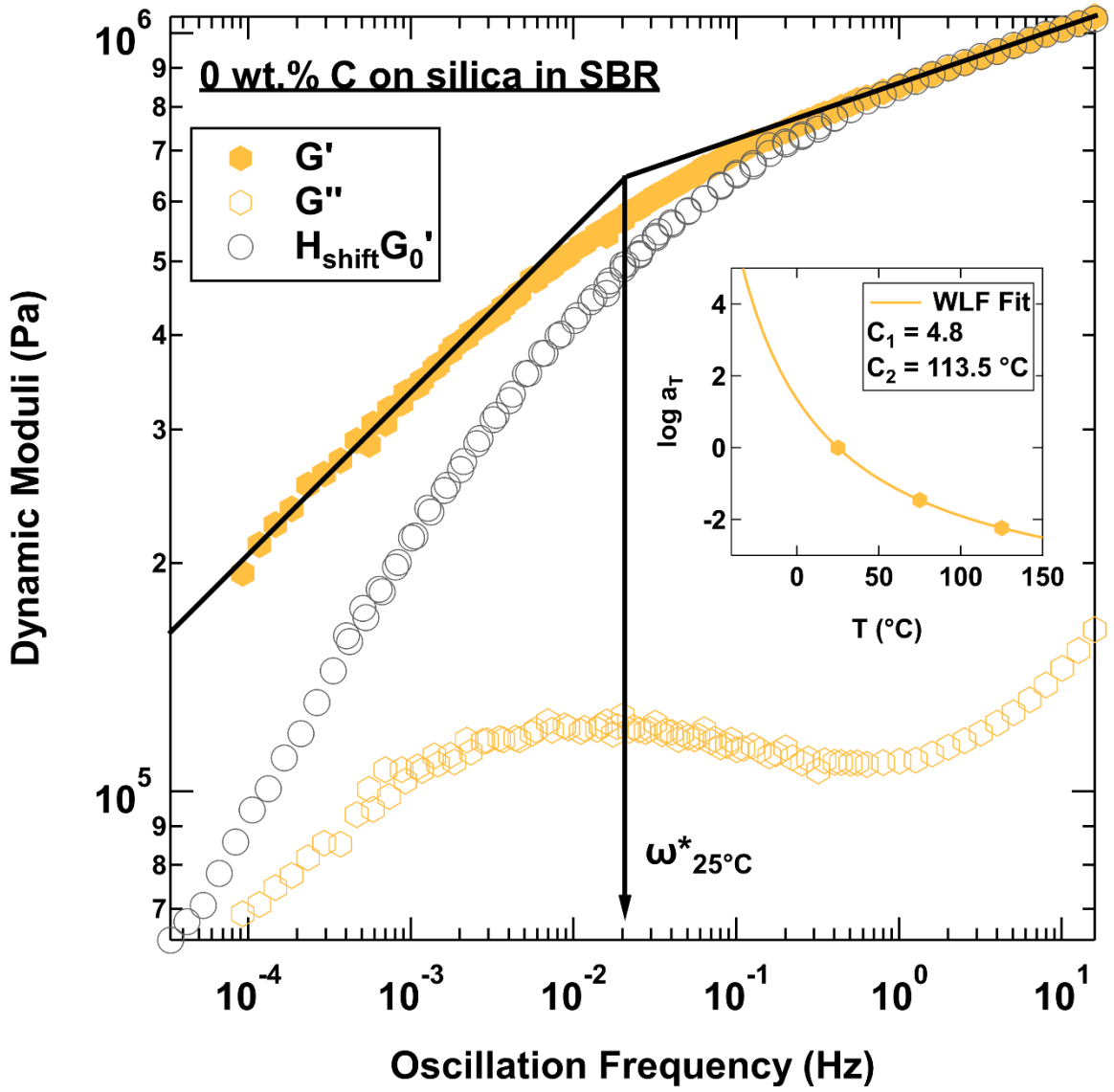

Figure S10. Plot of dynamic moduli, G' (storage) and G'' (loss) vs oscillation frequency, ω for the fumed silica with 0 wt.% surface carbon content at ϕ = 0.086 volume fraction filler (semi-dilute) in SBR at a reference temperature of 25°C. The storage modulus, $G_0{}'$, of the neat SBR rubber scaled by the hydrodynamic reinforcement factor, H_{shift}. Note that the master curves were constructed from isothermal frequency sweeps at 25°C, 75°C and 125°C. The experimental shift factors were fit using the WLF model to ascertain the constants, C_1 and C_2 as shown in the inset figure. The transition frequency ω^* i.e., the point on the frequency scale where the two storage moduli curves deviate is a characteristic frequency associated with the local filler network (Rishi et al., 2018).

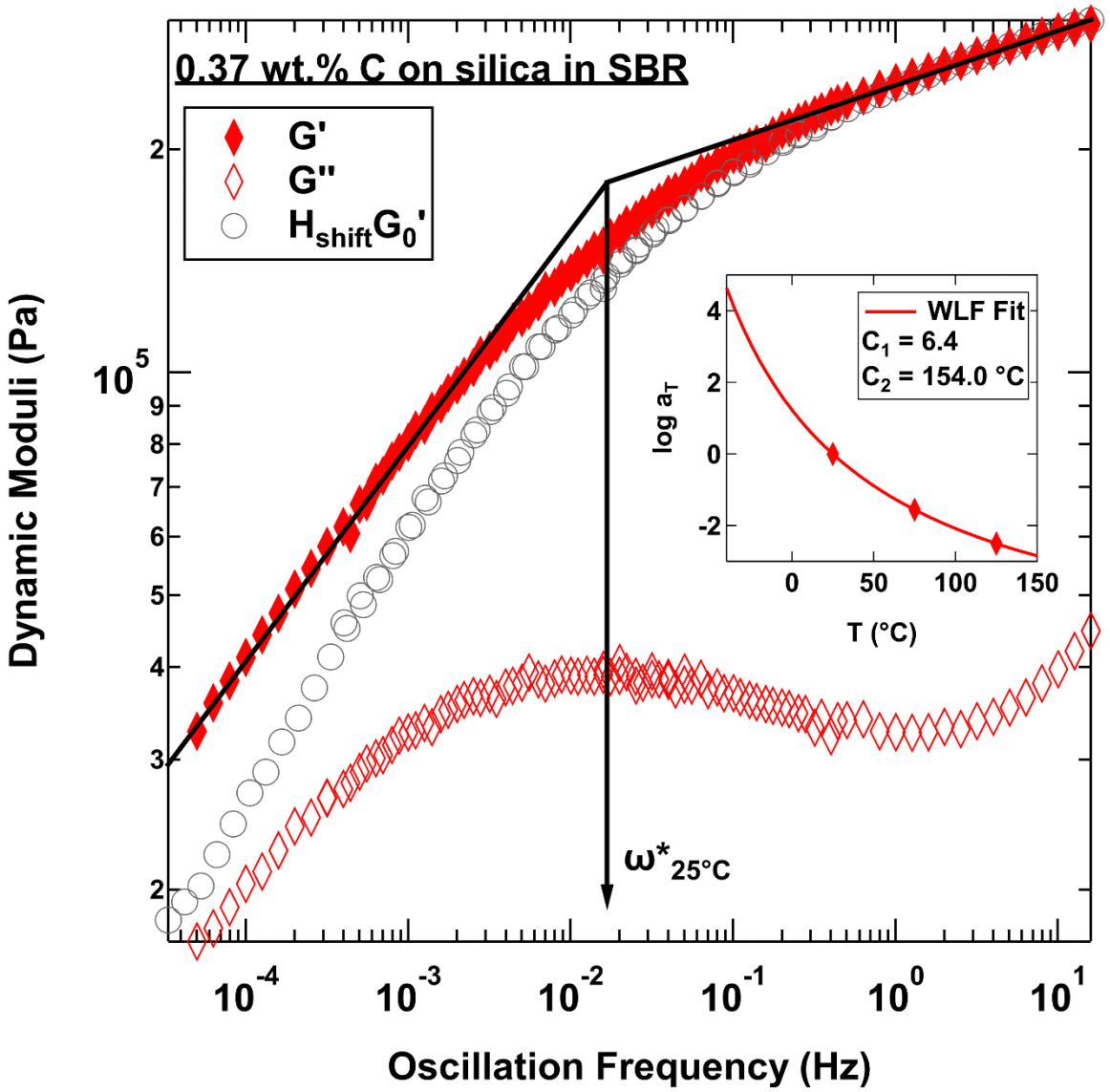

Figure S11. Plot of dynamic moduli, G' (storage) and G'' (loss) vs oscillation frequency, ω for the fumed silica with 0.37 wt.% surface carbon content at ϕ = 0.093 volume fraction filler (semi-dilute) in SBR at a reference temperature of 25°C. The storage modulus, ${G_0}'$, of the neat SBR rubber scaled by the hydrodynamic reinforcement factor, H_{shift}. Note that the master curves were constructed from isothermal frequency sweeps at 25°C, 75°C and 125°C. The experimental shift factors were fit using the WLF model to ascertain the constants, C_1 and C_2 as shown in the inset figure. The transition frequency ω^* i.e., the point on the frequency scale where the two storage moduli curves deviate is a characteristic frequency associated with the local filler network (Rishi et al., 2018).

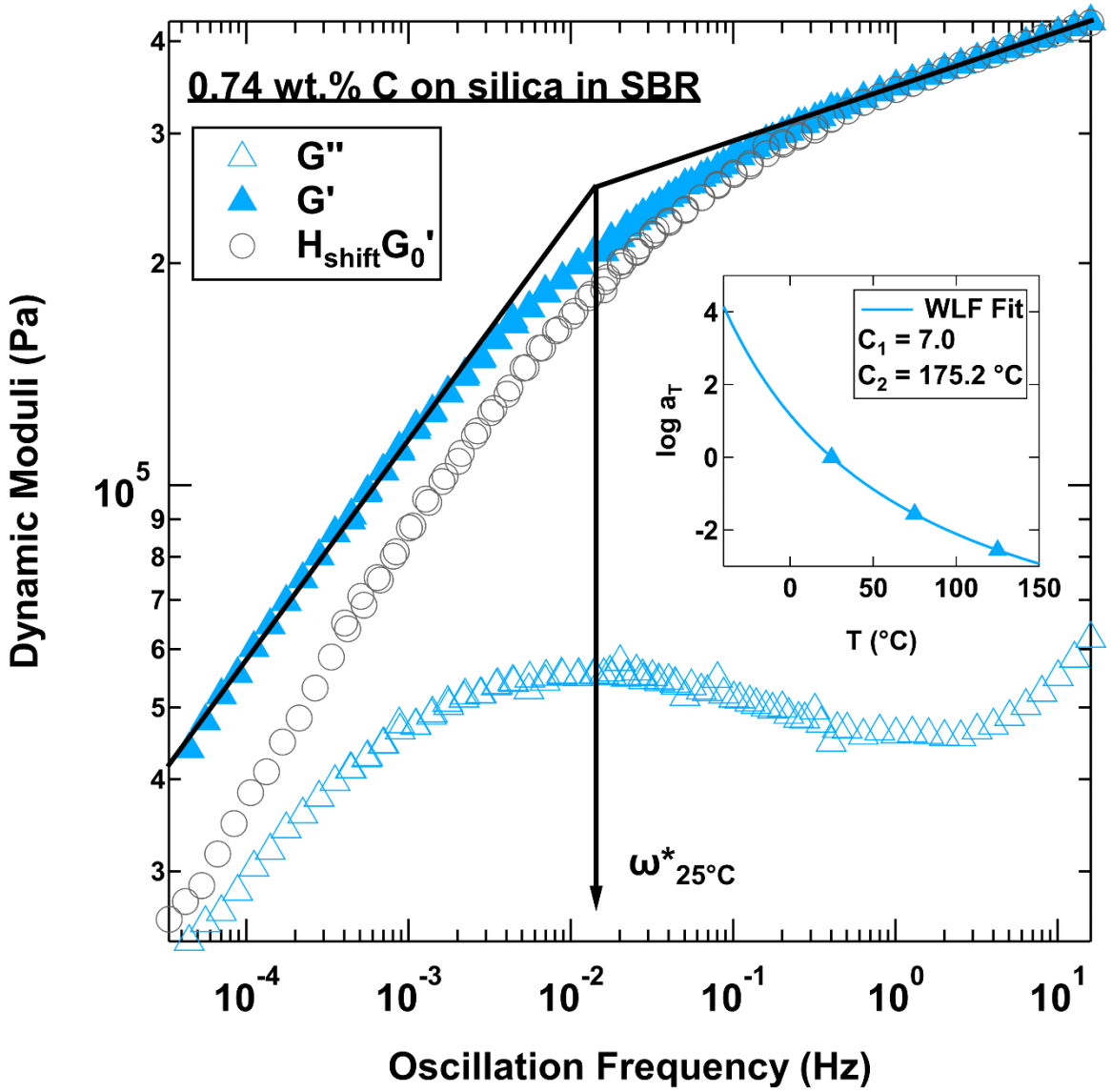

Figure S12. Plot of dynamic moduli, G' (storage) and G'' (loss) vs oscillation frequency, ω for the fumed silica with 0.74 wt.% surface carbon content at ϕ = 0.088 volume fraction filler (semi-dilute) in SBR at a reference temperature of 25°C. The storage modulus, ${G_0}'$, of the neat SBR rubber scaled by the hydrodynamic reinforcement factor, H_{shift}. Note that the master curves were constructed from isothermal frequency sweeps at 25°C, 75°C and 125°C. The experimental shift factors, a_T, were fit using the WLF model to ascertain the constants, C_1 and C_2 as shown in the inset figure. The transition frequency ω^* i.e., the point on the frequency scale where the two storage moduli curves deviate is a characteristic frequency associated with the local filler network (Rishi et al., 2018).

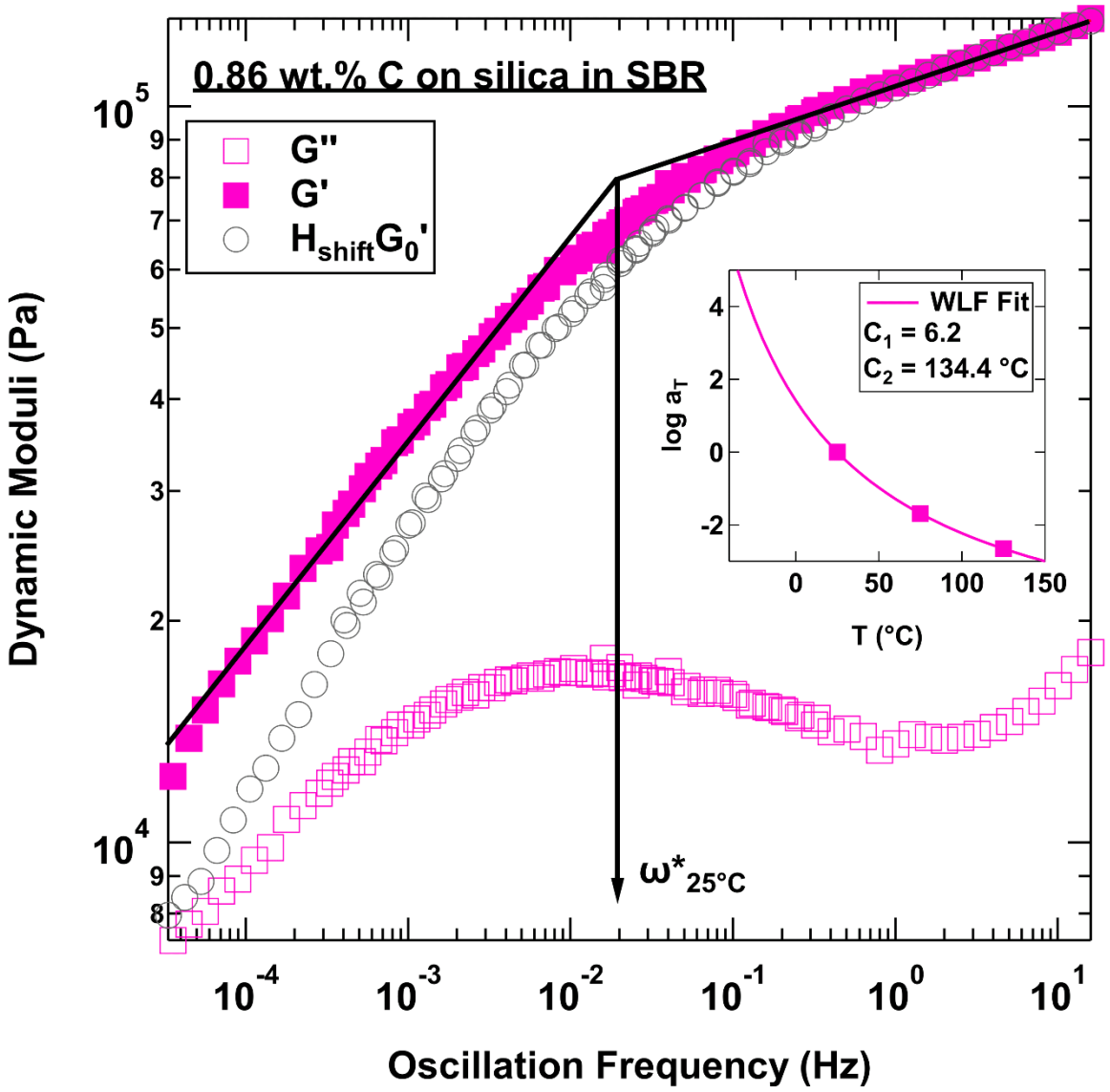

Figure S13. Plot of dynamic moduli, G' (storage) and G'' (loss) vs oscillation frequency, ω for the fumed silica with 0.86 wt.% surface carbon content at ϕ = 0.078 volume fraction filler (semi-dilute) in SBR at a reference temperature of 25°C. The storage modulus, $G_0{}'$, of the neat SBR rubber scaled by the hydrodynamic reinforcement factor, H_{shift}. Note that the master curves were constructed from isothermal frequency sweeps at 25°C, 75°C and 125°C. The experimental shift factors were fit using the WLF model to ascertain the constants, C_1 and C_2 as shown in the inset figure. The transition frequency ω^* i.e., the point on the frequency scale where the two storage moduli curves deviate is a characteristic frequency associated with the local filler network (Rishi et al., 2018).

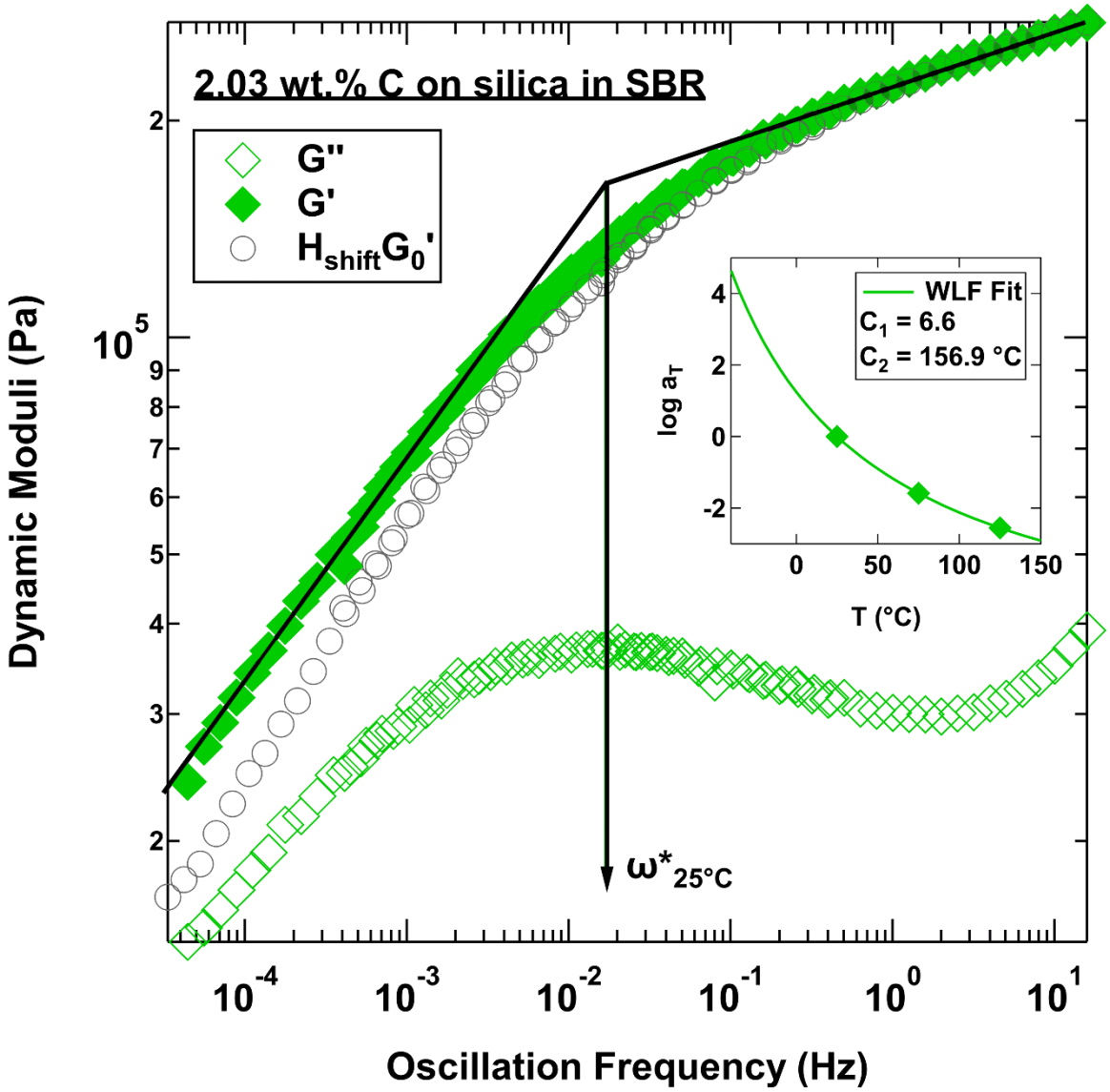

Figure S14. Plot of dynamic moduli, G' (storage) and G'' (loss) vs oscillation frequency, ω for the fumed silica with 2.03 wt.% surface carbon content at ϕ = 0.085 volume fraction filler (semi-dilute) in SBR at a reference temperature of 25°C. The storage modulus, ${G_0}'$, of the neat SBR rubber scaled by the hydrodynamic reinforcement factor, H_{shift}. Note that the master curves were constructed from isothermal frequency sweeps at 25°C, 75°C and 125°C. The experimental shift factors were fit using the WLF model to ascertain the constants, C_1 and C_2 as shown in the inset figure. The transition frequency ω^* i.e., the point on the frequency scale where the two storage moduli curves deviate is a characteristic frequency associated with the local filler network (Rishi et al., 2018).

Figure S15(a) shows that the relationship between and the transition time, τ^*, from rheology scale with the corresponding $1/c$ power-law slopes. Here c is the static aggregate connectivity dimension or the spectral dimension listed in Table 2 from scattering and the Unified fit. Note that, if one follows along the power-law slope, data points for lower concentration (smaller mesh size, ξ) would lie on the same line for any carbon coated silica nanofiller. Figure S15(b) is extracted from Figure S15(a) and shows that the filler network relaxation time is proportional to the surface carbon content. A similar plot is possible for the filler network mesh size as a function of carbon content. The relaxation time drops with higher carbon content while the mesh size increases. The carbon coating directly impacts the nature of the filler network structure and dynamics.

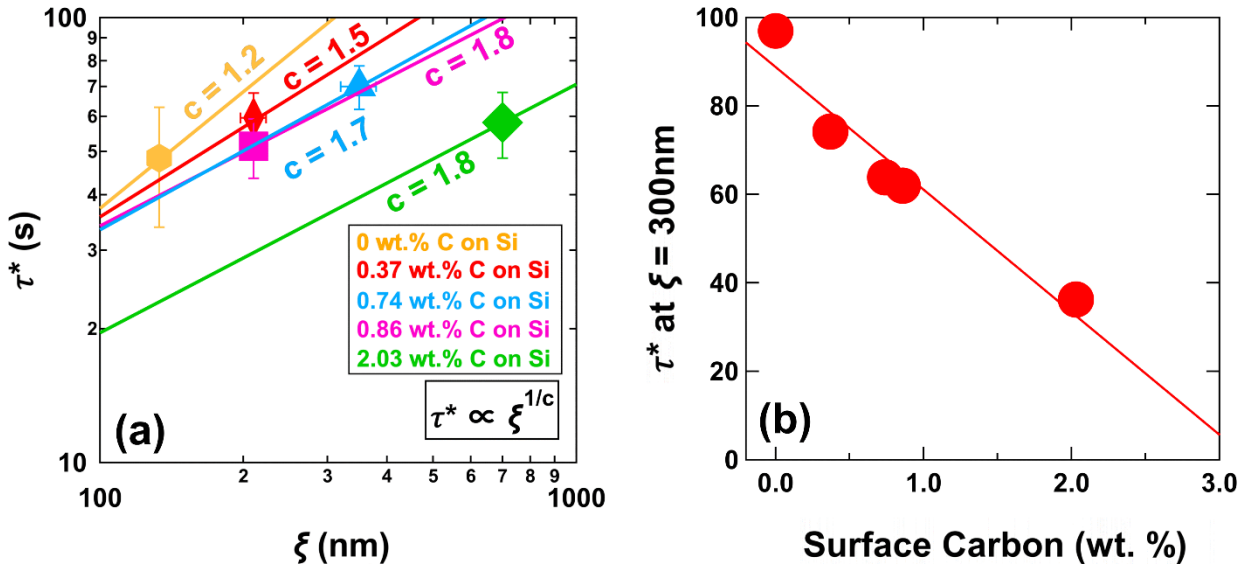

Figure S15. (a) Inverse transition frequency from dynamic rheology versus mesh size from USAXS for carbon coated silica nanofillers in SBR on a log-log scale. The inverse transition frequency, τ^*, is related to the mesh size, ξ, by reciprocal spectral dimension, which is equivalent to the static aggregate connectivity dimension, c, from scattering. Note that for each carbon coated silica the data point lies on the line corresponding to a slope of $1/c$ (Rishi et al., 2018). (b) τ^* versus weight percent surface carbon for a mesh size of 300nm from (a).

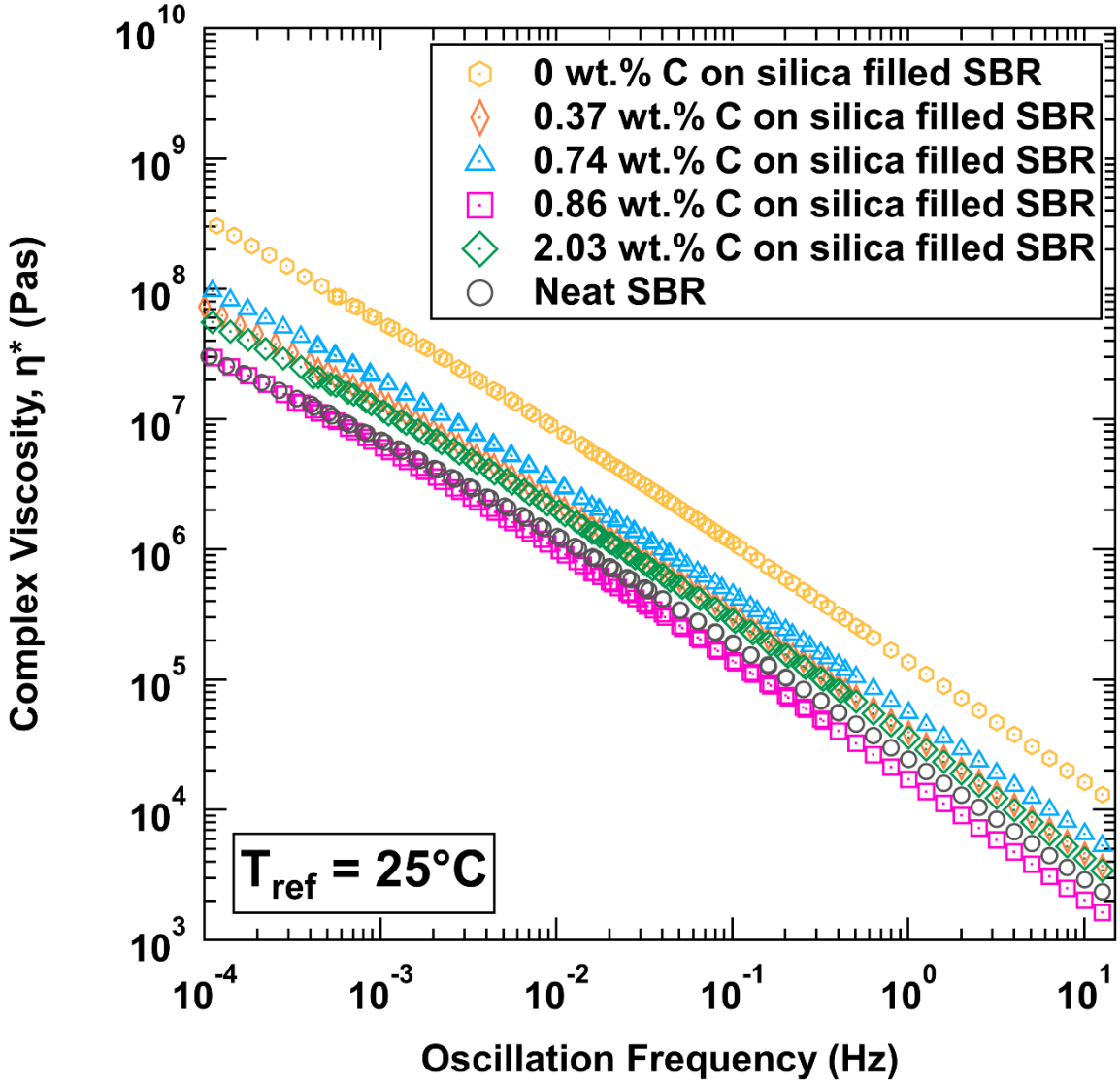

Figure S16. Complex viscosity, η^*, vs oscillation frequency (Hz) for the nanocomposite using fumed silica with 0 wt.%, 0.37 wt.%, 0.74 wt.%, 0.86 wt.%, and 2.03 wt.% surface carbon at ϕ = 0.086, 0.093, 0.088, 0.078, and 0.085 respectively, at a reference temperature of 25°C compared with the η^* of the neat SBR matrix.

Figures S17(a)-(e) shows plots of $\tan\delta$ as a function of frequency at 25°C for 0 wt.%, 0.37 wt.%, 0.74 wt.%, 0.86 wt.%, and 2.03 wt.% carbon-coated silica at $\phi \sim 0.09$ filler volume fraction in SBR. Since the master curves in Figures S10-S14 were constructed at a reference temperature of 25°C, the $\tan\delta$ at 0°C and 60°C can be computed from the inset horizontal shift factor, $\log a_T$ plots in theses master curve figures. The $\tan\delta$ values at the reference frequency, ω^*, associated with the local emergent structures characterized by a mesh size, ξ, ($\tau^* = 1/\omega^*$ versus ξ shown in Figure S15(a)) was used to determine the $\tan\delta$ values at 0°C and 60°C at the same reference frequency using time-temperature superposition.

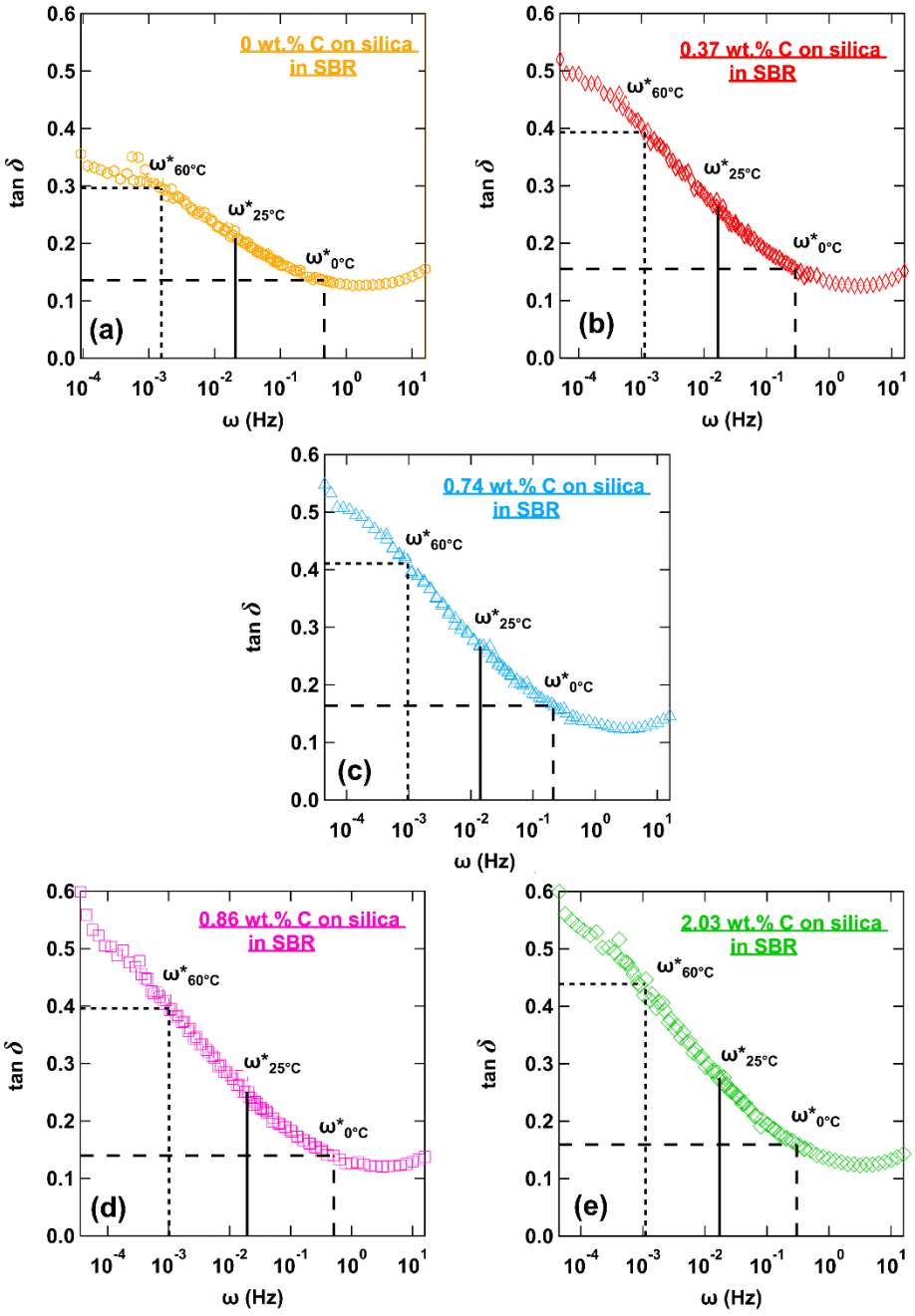

Figure S17. Plots of tan δ vs oscillation frequency (Hz) for the nanocomposite using fumed silica with (a) 0 wt.%, (b) 0.37 wt.%, (c) 0.74 wt.%, (d) 0.86 wt.%, and (e) 2.03 wt.% surface carbon and ϕ = (a) 0.086, (b) 0.093, (c) 0.088, (d) 0.078, and (e) 0.085 volume fraction filler respectively, at a reference temperature of 25°C. tan δ values at a reference frequency, ω^*, associated with the local emergent structure was used to determine the tan δ values at 0°C and 60°C at the same reference frequency using time-temperature superposition (Note that the horizontal shift factors at these two temperatures can be determined from Figures S10-S14 inset).

References

Beaucage, G. (1995). Approximations Leading to a Unified Exponential/Power-Law Approach to Small-Angle Scattering. *Journal of Applied Crystallography*, *28*(6), 717–728. https://doi.org/10.1107/S0021889895005292

Beaucage, G., & Schaefer, D. W. W. (1994). Structural studies of complex systems using small-angle scattering: a unified Guinier/power-law approach. *Journal of Non-Crystalline Solids*, *172–174*, 797–805. https://doi.org/DOI: 10.1016/0022-3093(94)90581-9

Brinker, C. J., & Scherer, G. W. (1990). *Sol–gel Science. The Physics and Chemistry of Sol– gel Processing*. Academic Press.

Duran, A., Serna, C., Fornes, V., & Fernandez Navarro, J. M. (1986). Structural considerations about SiO2 glasses prepared by sol-gel. *Journal of Non-Crystalline Solids*, *82*(1–3), 69–77. https://doi.org/10.1016/0022-3093(86)90112-2

Gottardi, V., Guglielmi, M., Bertoluzza, A., Fagnano, C., & Morelli, M. A. (1984). Further investigations on Raman spectra of silica gel evolving toward glass. *Journal of Non-Crystalline Solids*, *63*(1–2), 71–80. https://doi.org/10.1016/0022-3093(84)90387-9

Kammler, H. K., Mueller, R., Senn, O., & Pratsinis, S. E. (2001). Synthesis of silica-carbon particles in a turbulent H2-air flame aerosol reactor. *AIChE Journal*, *47*(7), 1533–1543. https://doi.org/10.1002/aic.690470707

McDonald, R. S. (1958). Surface functionality of amorphous silica by infrared spectroscopy. *Journal of Physical Chemistry*, *62*(10), 1168–1178. https://doi.org/10.1021/j150568a004

Mueller, R., Kammler, H. K., Pratsinis, S. E., Vital, A., Beaucage, G., & Burtscher, P. (2004). Non-agglomerated dry silica nanoparticles. *Powder Technology*, *140*(1–2), 40–48. https://doi.org/10.1016/j.powtec.2004.01.004

Mueller, R., Kammler, H. K., Wegner, K., & Pratsinis, S. E. (2003). OH Surface Density of SiO 2 and TiO 2 by Thermogravimetric Analysis. *Langmuir*, *19*(1), 160–165. https://doi.org/10.1021/la025785w

Mulderig, A., Beaucage, G., Vogtt, K., Jiang, H., & Kuppa, V. (2017). Quantification of branching in fumed silica. *Journal of Aerosol Science*, *109*(March), 28–37. https://doi.org/10.1016/j.jaerosci.2017.04.001

Rishi, K., Beaucage, G., Kuppa, V., Mulderig, A., Narayanan, V., McGlasson, A., Rackaitis, M., & Ilavsky, J. (2018). Impact of an Emergent Hierarchical Filler Network on Nanocomposite Dynamics. *Macromolecules*, *51*(20), 7893–7904. https://doi.org/10.1021/acs.macromol.8b01510

Rishi, K., Pallerla, L., Beaucage, G., & Tang, A. (2020). Dispersion of surface-modified, aggregated, fumed silica in polymer nanocomposites. *Journal of Applied Physics*, *127*(17), 174702. https://doi.org/10.1063/1.5144252